Journal of Advances in Modeling Earth Systems

RESEARCH ARTICLE
10.1029/2018MS001305

Key Points:
- Warm season convection-permitting climate simulations reproduced the observed characteristics of mesoscale convective systems
- Macrophysical properties of simulated mesoscale convective systems are sensitive to microphysics parameterizations
- Microphysics parameterizations that produce more stratiform rainfall favor longer-lived convection through stronger dynamical feedbacks

Supporting Information:
- Supporting Information S1

Correspondence to:
Z. Feng,
zhe.feng@pnnl.gov

Citation:
Feng, Z., Leung, L. R., Houze, R. A., Jr., Hagos, S., Hardin, J., Yang, Q., et al. (2018). Structure and evolution of mesoscale convective systems: Sensitivity to cloud microphysics in convection-permitting simulations over the United States. *Journal of Advances in Modeling Earth Systems*, *10*, 1470–1494. https://doi.org/10.1029/2018MS001305

Received 28 FEB 2018
Accepted 12 JUN 2018
Accepted article online 19 JUN 2018
Published online 5 JUL 2018

©2018. The Authors.
This is an open access article under the terms of the Creative Commons Attribution-NonCommercial-NoDerivs License, which permits use and distribution in any medium, provided the original work is properly cited, the use is non-commercial and no modifications or adaptations are made.

Structure and Evolution of Mesoscale Convective Systems: Sensitivity to Cloud Microphysics in Convection-Permitting Simulations Over the United States

Zhe Feng[1], L. Ruby Leung[1], Robert A. Houze Jr.[1,2], Samson Hagos[1], Joseph Hardin[1], Qing Yang[1], Bin Han[3], and Jiwen Fan[1]

[1]Pacific Northwest National Laboratory, Richland, WA, USA, [2]Department of Atmospheric Sciences, University of Washington, Seattle, WA, USA, [3]School of Atmospheric Sciences, Nanjing University, Nanjing, China

Abstract Regional climate simulations over the continental United States were conducted for the 2011 warm season using the Weather Research and Forecasting model at convection-permitting resolution (4 km) with two commonly used microphysics parameterizations (Thompson and Morrison). Sensitivities of the simulated mesoscale convective system (MCS) properties and feedbacks to large-scale environments are systematically examined against high-resolution geostationary satellite and 3-D mosaic radar observations. MCS precipitation including precipitation amount, diurnal cycle, and distribution of hourly precipitation intensity are reasonably captured by the two simulations despite significant differences in their simulated MCS properties. In general, the Thompson simulation produces better agreement with observations for MCS upper level cloud shield and precipitation area, convective feature horizontal and vertical extents, and partitioning between convective and stratiform precipitation. More importantly, Thompson simulates more stratiform rainfall, which agrees better with observations and results in top-heavier heating profiles from robust MCSs compared to Morrison. A stronger dynamical feedback to the large-scale environment is therefore seen in Thompson, wherein an enhanced mesoscale vortex behind the MCS strengthens the synoptic-scale trough and promotes advection of cool and dry air into the rear of the MCS region. The latter prolongs the MCS lifetimes in the Thompson relative to the Morrison simulations. Hence, different treatment of cloud microphysics not only alters MCS convective-scale dynamics but also has significant impacts on their macrophysical properties such as lifetime and precipitation. As long-lived MCSs produced 2–3 times the amount of rainfall compared to short-lived ones, cloud microphysics parameterizations have profound impact in simulating extreme precipitation and the hydrologic cycle.

Plain Language Summary Massive thunderstorms over the Great Plains of the United States have become more frequent and more intense in the past decades. As Earth continues to warm, changes in the characteristics of these massive thunderstorms, which often cause flooding and severe wind damage, have major societal implications. Climate models with spatial resolution comparable to weather forecasting models can now be used to simulate the complex physics in storms and reproduce their climatological properties. However, details of how to represent the cloud microphysical processes remain uncertain, with potential implications for long-term simulation of climate in regions of convective storms. This study examines the uncertainties associated with cloud microphysics of convective storms in the central United States by using two different microphysical representations and comparing results with a warm-season satellite and radar observations. Microphysical processes leading to a broader and more realistic storm rainfall areas favor prolonged lifetime of the storms and thus have greater effects on the evolution of the large-scale circulation and greater potential for storms producing floods, factors important for evaluating the effects of convective storms in a changing climate.

1. Introduction

Mesoscale convective systems (MCSs) are the largest form of cumulonimbus cloud complex that develops when convection aggregates and grows upscale, forming mesoscale circulations that organize the convection. They can reach horizontal dimensions of hundreds to a thousand kilometer and can last up to 24 hr (Houze, 2004). MCSs consist of active convective towers and expansive stratiform regions (Houze et al., 1980), which differentiate these convective systems from isolated thunderstorms. MCSs play an important role in the climate system as they produce abundant rainfall and redistribute energy in the atmosphere,

shaping the general circulation of our climate system. In the tropics, 40–60% of rainfall produced by MCSs is associated with the stratiform region (Cheng & Houze, 1979; Schumacher & Houze, 2003; Virts & Houze, 2015). As a result, the net latent heating profile of MCSs is generally more "top heavy," so MCSs have larger impacts on the upper level circulation than isolated convection (Fritsch et al., 1994; Hartmann et al., 1984; Schumacher et al., 2004).

MCS also play an important role in the hydrological cycle of the midlatitudes. For example, in the central United States, MCSs contribute between 30% and 70% of warm season rainfall (Feng et al., 2016; Fritsch et al., 1986; Nesbitt et al., 2006). Long-lasting MCSs are responsible for a majority of flood-producing extreme rainfall events (Schumacher & Johnson, 2006; Stevenson & Schumacher, 2014) and contribute to severe weather phenomena (Bentley & Mote, 1998; Bentley & Sparks, 2003; Houze et al., 1990). In recent decades, increased frequency and intensity of long-lived MCSs have coincided with an upward trend in springtime total and extreme rainfall in the central United States (Feng et al., 2016). It follows that understanding changes in future extreme rainfall in regions frequented by MCSs hinges upon accurate model representation of the large-scale circulation and mesoscale convective processes controlling these organized convective systems.

General circulation models (GCMs) have a long history of summertime warm and dry bias over the central United States (Cheruy et al., 2014; Klein et al., 2006; Morcrette et al., 2018). Lin et al. (2017) found that the persistent warm bias in most Coupled Model Intercomparison Project Phase 5 simulations was preceded by precipitation deficit arising from the model's failure in capturing heavy precipitation events, which are mostly produced by MCSs that frequently initiate in late afternoon, with precipitation peaking during nocturnal hours (Carbone et al., 2002). Most current GCMs do not yet represent MCSs because convection in these coarse resolution models is parameterized with no explicit consideration of the mesoscale processes characterizing MCSs. As a result, global and regional climate models with parameterized convection largely fail to simulate major precipitation events (Bukovsky & Karoly, 2010; Kooperman et al., 2014; Lin et al., 2017) and their associated diurnal signature (Dai, 2006; Gustafson et al., 2014). Such persistent biases in simulating warm season heavy precipitation by climate models significantly undermine our confidence in their projected extreme rainfall in the changing climate.

Recent advancements in computational resources have allowed regional climate model simulations to be run at convection-permitting resolutions ($\lesssim$4-km grid spacing), bypassing the need for convection parameterizations. Compared to models with parameterized convection, convection-permitting models (CPMs) produce more realistic timing and magnitude of summertime precipitation diurnal cycle (Ban et al., 2014; Gao et al., 2017) and better representation of high intensity precipitation features (PFs) and extreme hourly precipitation statistics (Kendon et al., 2012). Resolving convection in long simulations by CPMs provides the ability to represent interactions between convection and the large-scale circulations in an evolving climate. Such interactions are important because MCSs interact strongly with their large-scale environments. Yang et al. (2017) showed that long-lived MCSs not only produced more overall heating but also distribute the heating to higher levels of the atmosphere. Potential vorticity generated in midlevels by these top-heavy heating profiles tends to promote or strengthen midlevel mesoscale convective vortexes (MCVs) that may strengthen the synoptic-scale trough, enhancing dry air intrusion and evaporative cooling behind the MCS region, help maintain the longevity of MCSs, and alter the evolution of the large-scale circulation.

While CPMs are able to simulate mesoscale and some convective scale processes, significant challenges and uncertainties remain in their applications in climate modeling. At convection-permitting resolution, cloud microphysics, boundary layer processes, and turbulence can contribute to model uncertainty. In this study, we focus on uncertainty associated with the representation of cloud microphysics. Studies comparing remote sensing and in situ observations with CPM simulations of MCSs show consistent high biases in ice hydrometeor size and their associated radar reflectivity across many commonly used microphysics parameterizations (Stanford et al., 2017; Varble, Zipser, Fridlind, Zhu, Ackerman, Chaboureau, Collis, et al., 2014b). Comparison of model output to dual-Doppler radar retrievals in both tropical maritime and midlatitude continental convection indicates that simulated convective-scale updraft intensities in MCSs are systematically too strong, and stratiform region area and rainfall are consistently underestimated across almost all microphysics parameterizations (Fan et al., 2017; Varble, Zipser, Fridlind, Zhu, Ackerman, Chaboureau, Fan, et al., 2014a). Because high-quality simultaneous remote sensing and in situ observations of MCSs are difficult to obtain, they are

only available from limited-duration field campaigns. Therefore, most previous studies evaluating the process level performance of CPMs in simulating MCSs are limited to case studies for well observed events, leaving a gap in evaluation of MCS statistics in convection permitting regional climate simulations.

Recently, Prein et al. (2017) analyzed model MCSs in a 13-yearlong CPM (4-km grid spacing) regional climate simulation over the eastern United States performed with the Weather Research and Forecasting (WRF) model (Skamarock et al., 2008). MCSs were identified and tracked by using simulated hourly precipitation and evaluated against a radar-based precipitation data set. Their simulations captured many observed MCS PF characteristics such as lifetime, size, precipitation intensity, and propagation speed, but MCS frequency was significantly underestimated in the central United States during late summer. Given the limitation of using only precipitation to characterize MCSs, Prein et al. (2017) did not evaluate the realism of internal structures of the MCSs in their simulations or consider sensitivity of their results to microphysics parameterizations. More systematic evaluation of CPM simulated MCS three-dimensional (3D) structures, their interactions with large-scale environments and sensitivities to microphysics parameterizations are needed to understand the uncertainties associated with microphysical schemes employed in climate simulations using CPMs. Further, while 4-km grid spacing CPM may be able to resolve mesoscale features associated with MCSs, the effective resolution (typically about seven horizontal grid spacing; e.g., Skamarock, 2004) is insufficient to resolve turbulence. Bryan and Morrison (2012) showed that idealized squall line simulations are sensitive to horizontal grid spacing partly because turbulence development can be better resolved with 250-m horizontal grid spacing. Representing and parameterizing turbulence and their effects in CPM simulations remains a challenge. More detail discussions related to this topic can be found in section 5.3 of Prein et al. (2015).

In this study, we evaluate the capability of CPM in reproducing the observed warm season MCS properties in the central United States, including their structure and life cycle, propagation, and interaction with large-scale environments, and examine the sensitivities of these aspects to the choice of microphysics parameterizations. In a regional climate modeling framework that uses the WRF model, we compare WRF MCS population statistics to observations that are based not simply on precipitation data but rather on MCS identification and tracking that combines two high-resolution observation data sets, geostationary satellite infrared brightness temperature, and 3-D Next-Generation Radar (NEXRAD) mosaic along with the precipitation. The latter is important for understanding the interactions between MCSs and the circulation and hence the role of MCSs in the climate system. To represent the range of uncertainty associated with microphysical representations, we run simulations with two widely used microphysical schemes (Morrison et al., 2009; Thompson et al., 2008). Although the two schemes are known to generally produce realistic results in the WRF modeling framework, there are fundamental differences that can lead to different cloud and precipitation structures. By elucidating differences in macrophysical characteristics of MCS that result from the choice of cloud microphysical parameterization scheme, we demonstrate linkages between the MCS characteristics and the feedback from MCSs to the large-scale circulation that have important implications for climate modeling. Section 2 describes the model simulation setup and observation data set used in this study. Section 3 provides details of the algorithm in identifying and tracking robust MCSs. Various aspects of the simulated MCSs and how they interact with the environment are evaluated and presented in section 4. Finally, summary and discussion of future efforts are given in section 5.

2. Model Setup and Observations

2.1. Model Setup

The WRF model (Skamarock et al., 2008) version 3.6.1 was used in this study. The model configuration was similar to that used in Yang et al. (2017) and is listed in Table 1. A 4-km horizontal grid spacing and 65 vertical levels from the surface to 50 hPa were used. The model domain covers most of the contiguous United States from 28°N to 50°N and 120°W to 75°W (Figure 1a). The initial and lateral boundary conditions, including land surface conditions, were provided by Global Forecast System reanalysis data. The lateral boundary forcing was updated every 6 hr. No interior nudging was applied to the simulations to allow interactions between MCSs and their large-scale environments to be examined. The model output was archived at 1-hourly frequency to facilitate tracking of MCSs. Two sets of simulations were conducted from 1 May to 31 August 2011 with identical configurations except for the microphysics. Two commonly used two-moment

Table 1
Boundary Conditions and Physics Parameterizations Used in the WRF Model Setup

Simulation period	1 May 2011 to 31 August 2011
Lateral and surface forcing	Global Forecast System Reanalysis
PBL scheme	YSU (Hong et al., 2006)
Surface scheme	MM5 (Beljaars, 1995)
Land surface model	Noah Land Surface model (Tewari et al., 2004)
Longwave radiation scheme	RRTMG (Iacono et al., 2000)
Shortwave radiation scheme	Goddard shortwave scheme (Chou & Suarez, 1999)
Microphysics	Morrison 2-moment (Morrison et al., 2009) Thompson (Thompson et al., 2008)

microphysics schemes with similar complexity were chosen for this study: Morrison et al. (2009) and Thompson et al. (2008). Both schemes predict the number and mixing ratios of cloud ice and rain and the mixing ratio of cloud droplets, but they differ significantly in their treatments of snow and graupel/hail in terms of double versus single moment and the shape of the particle size distributions (PSDs). More details about the hydrometeor size distribution assumptions in these two schemes, and associated mass-dimension relationships and sedimentation speeds, are provided in the Appendix in the Supporting Information. The model was initialized at 0600 UTC 1 May 2011 and integrated continuously over the 4-month period.

2.2. Observations

A global merged geostationary satellite 11.5-μm infrared brightness temperature (T_b) data set was used in this study for identifying and tracking MCSs. The satellite data set was produced by the Climate Prediction Center and National Centers for Environmental Prediction (Janowiak et al., 2001). The satellite T_b data set has an approximate 4-km spatial resolution and 30-min temporal resolution.

Depiction of 3-D storm structures and associated precipitation were provided by the National Mosaic and Multi-Sensor Quantitative Precipitation Estimations (NMQ) 3-D reflectivity mosaic data, produced by the National Severe Storm Laboratory (Zhang et al., 2011). Radar reflectivity data from individual NEXRAD were quality-controlled and objectively merged to a gridded 3-D national mosaic radar data set. The NMQ reflectivity data have a 0.01°(~1 km) spatial resolution, 31 vertical levels from 0.5 and 18 km, and 5-min temporal resolution.

While the NMQ data set was produced for the entire contiguous United States, only data from 110°W to 80°W and 20°N to 50°N were used in this study. We focused our effort in the central United States (red box in Figure 1) because a majority of MCSs and associated precipitation concentrate in this region (Feng et al.,

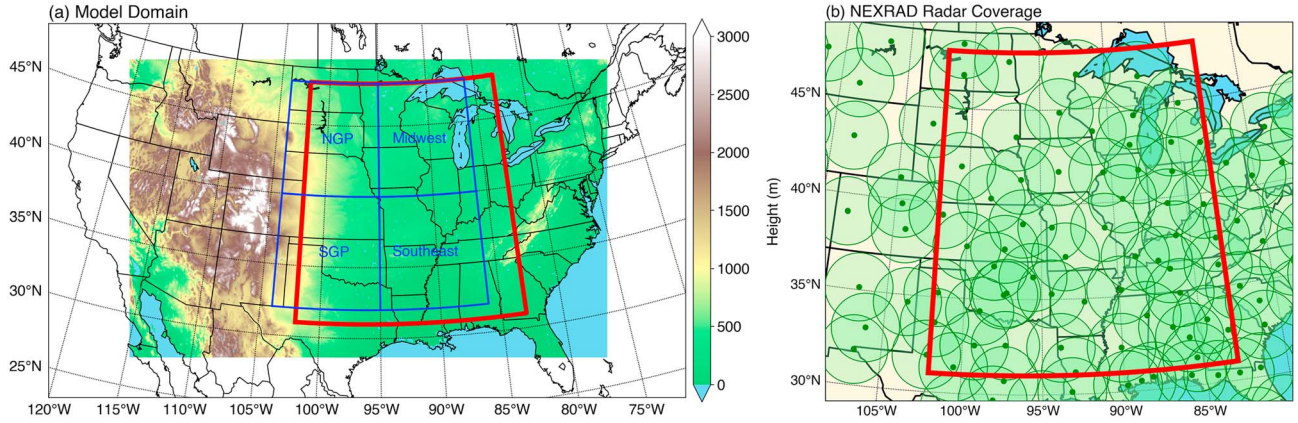

Figure 1. (a) The model domain used in this study. The color shadings are the model terrain height. (b) Next-Generation Radar (NEXRAD) radar coverage in central U.S. The green dots denote individual NEXRAD radar locations, and the filled circles are approximately 180 km radius from each radar. The overlap area of the circles has multiple NEXRAD radar coverage. Note that lowest-level scans from NEXRAD can reach further than 180 km to provide baseline coverage in radar sparse area but with lower resolution. The red box shows the central U.S. area of focus in this study. The four blue box regions in (a) show four subregions in Figure 8.

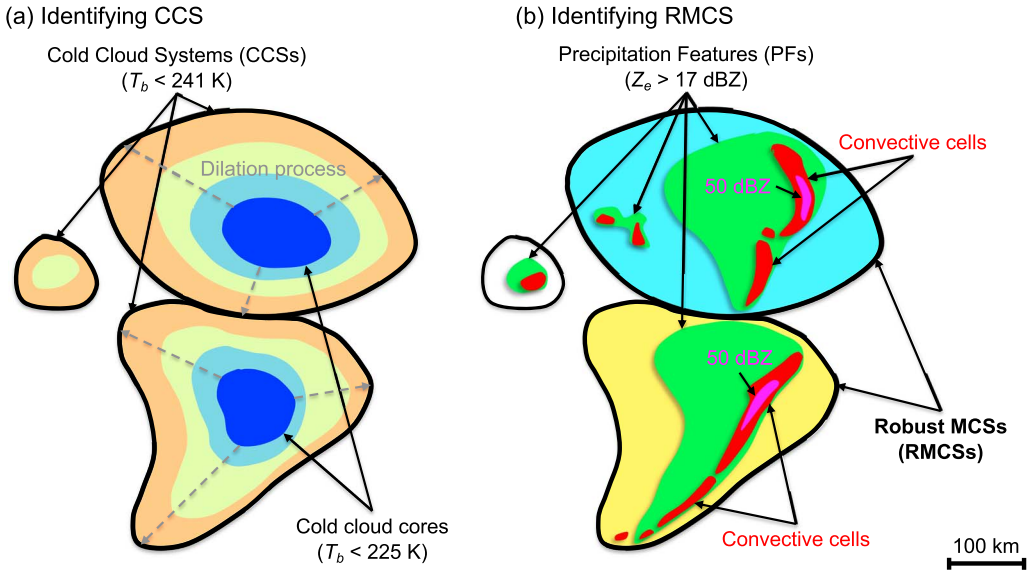

Figure 2. Schematic to illustrate identification of robust mesoscale convective system (RMCS). (a) Cold cloud systems (CCS) are identified using satellite T_b data. The thick black contours show the 241 K outline of CCS. The cold cloud cores ($T_b < 225$ K) shown in blue patches are dilated outward to 241 K to separate CCS with distinct cold cloud cores. (b) Precipitation features (PFs) within the CCS are identified with contiguous area of radar reflectivity >17 dBZ at 2.5 km height. PF major axis length and convective cells with imbedded 50-dBZ echoes anywhere within the PF are used to identify RMCS. The two colored patches in (b) with thick black outlines denote two RMCSs.

2016; Fritsch et al., 1986). The central U.S. region has relatively flat terrain and good radar coverage. Many areas have multiple radar coverage that improves characterization of both near surface precipitation and upper level storm structures (Zhang et al., 2011). The NMQ radar data were averaged to the 4-km satellite grid to facilitate tracking of MCSs.

Quantitative precipitation estimate is also available in the NMQ data set. The Q2 precipitation product, as part of the NMQ system, combines NEXRAD radar quantitative precipitation estimate and surface rain gauge network data. The 1-hourly Q2 precipitation data set used in this study has been bias-corrected with rain gauge network data. The Q2 precipitation data set is provided at 0.01°(~1 km) spatial resolution. The precipitation data were also averaged to the 4-km satellite grid.

3. Identifying and Tracking MCSs

3.1. Cloud Tracking Using Satellite Data

Cold cloud systems (CCSs) associated with deep convective clouds were identified using the satellite Tb data. An updated CCS identification method based on that used by Feng et al. (2016) and Yang et al. (2017) was developed in this study. Rather than identifying CCS with contiguous satellite pixels with $T_b < 241$ K, this study included additional criteria to better separate nearby CCSs that have distinct cold cloud cores associated with separate convective cloud clusters. This method is similar to the MCS identification method of Yuan and Houze (2010) in that infrared temperature contours are used to find separate cold centers and rain areas with higher intensity cores are identified.

First, a box smoothing with a window size of 10 × 10 pixels (equivalent to 40 km × 40 km) was applied to the T_b field. Contiguous areas with the smoothed $T_b < 225$ K were identified as distinct CCSs with a cold cloud core (Figure 2a). The smoothing procedure prevents over segmentation of cloud systems, but the size of the smoothing window may need to be adjusted for data sets of different resolutions. We visually examined a variety of different complex observed cloud scenes with multiple convective systems nearby; the 10 × 10 pixel smoothing window seems to provide the most reasonable segregation of cloud systems mimicking a subjective decision. Next, each CCS was expanded outward through a dilation process until the unsmoothed T_b reaches 241 K. A 1-pixel dilation was applied to the largest cloud clusters in a scene followed by the second

largest cluster, and so on. By doing so, we assumed that larger deep convective systems produce more detrained upper level clouds than smaller ones; hence, surrounding warmer cloud pixels are preferentially grouped to the larger cloud systems. Finally, after all CCSs with cold cloud core were dilated to 241 K, the remaining clouds with $T_b < 241$ K but without a cold cloud core were labeled following the same procedure as Feng et al. (2016; thick black contours in Figure 2a).

Cold cloud systems were tracked by using an automated objective tracking method described in detail by Feng et al. (2012). The tracking method is based on overlapping of CCSs between two consecutive time steps to determine if they are the same one. Identification of MCSs using tracked CCSs from satellite T_b data followed Fritsch et al. (1986) and Feng et al. (2016): a CCS with an area exceeding 6×10^4 km^2 and persists for at least 6 hr is considered a potential MCS. Because collocated NEXRAD radar data are available, we applied additional radar-based criteria (described below) to further identify robust MCSs. Smaller CCSs that last <6 hr and merge with or split from a CCS-identified MCS are considered part of the tracked MCS. This updated MCS tracking algorithm is referred to as FLEXible object TRacKeR (FLEXTRKR).

To better match with hourly WRF output, only the hourly satellite and radar data were used in this study. While the satellite/radar data represent instantaneous snapshots, the Q2 precipitation data represent hourly accumulation (e.g., 1200 UTC Q2 precipitation is accumulation from 1100 UTC to 1159 UTC). Therefore, some spatial shift is possible within an hour between the instantaneous radar reflectivity field and the precipitation field, considering the propagating nature of MCSs. The FLEXTRKR described above were applied to the WRF simulated outgoing longwave radiation data. The WRF outgoing longwave radiation data were converted to equivalent infrared T_b following the empirical formulation provided by Yang and Slingo (2001). The WRF simulated precipitation is also calculated as hourly accumulation and subjected to the same treatment as applied to observations.

3.2. Storm Structures Identified by Radar Data

The NMQ 3-D reflectivity data provide more detailed MCS structures associated with the tracked CCSs. PFs underneath the MCS cloud shield were identified using the Q2 precipitation data set. A PF is defined as a contiguous area with precipitation exceeding 1 mm hr^{-1} and reflectivity larger than 17 dBZ at 2.5-km height (Figure 2b). The 17-dBZ threshold was chosen to be consistent with studies using Tropical Rainfall Measuring Mission radar data (e.g., Houze et al., 2015). An MCS could contain multiple PFs in this study, particularly during the initial development stage when multiple convective clusters begin to aggregate. Propagation speed and direction of the MCSs were calculated using the PFs. The 2.5-km reflectivity fields in the largest five PFs associated with a MCS between two time steps were used to calculate a 2-D cross-correlation map. The index of the maximum value of the correlation map gives the number of pixels the MCS advected in the east-west/north-south directions between time steps. Given the advection distance and time lag, a propagation speed can then be calculated. The advantage of using the full 2-D reflectivity field to estimate propagation speed compared to simply using the center is that it is much less prone to changes in the shape of the PF. The morphological changes of the PF shapes could result in large shifts in the center location and subsequent errors in the estimates of propagation speed.

Convective and stratiform precipitation in a PF were further separated by applying the radar reflectivity texture classification technique of Steiner et al. (1995) with thresholds tuned for midlatitude warm season convection (Feng et al., 2011). Reflectivity at a constant 2.5-km height was used for the classification. Contiguous convective precipitation pixels were grouped and labeled as a convective cell (Figure 2b). Various thresholds of radar echo-top heights (e.g., 10 and 40 dBZ) in a convective cell were calculated as proxies for the intensity of convection (e.g., Zipser et al., 2006) and saved for further analysis. In addition, convective cells and stratiform rain region characteristics such as major axis length and area were also obtained for each tracked MCS. The same radar data processing procedure described above was applied to the WRF model simulated 10-cm wavelength radar reflectivity equivalent to the NEXRAD observed reflectivity. The WRF model simulated radar reflectivity field was vertically regridded to a constant 0.5-km height resolution before the radar processing routine was applied.

Figure 3 shows an example of an MCS inferred from radar observations and the WRF simulations using two different microphysics schemes. An intense MCS (squall line) with large leading convective-line trailing stratiform area was observed between the borders of Oklahoma, Arkansas, and Texas at 00 UTC 21 May 2011.

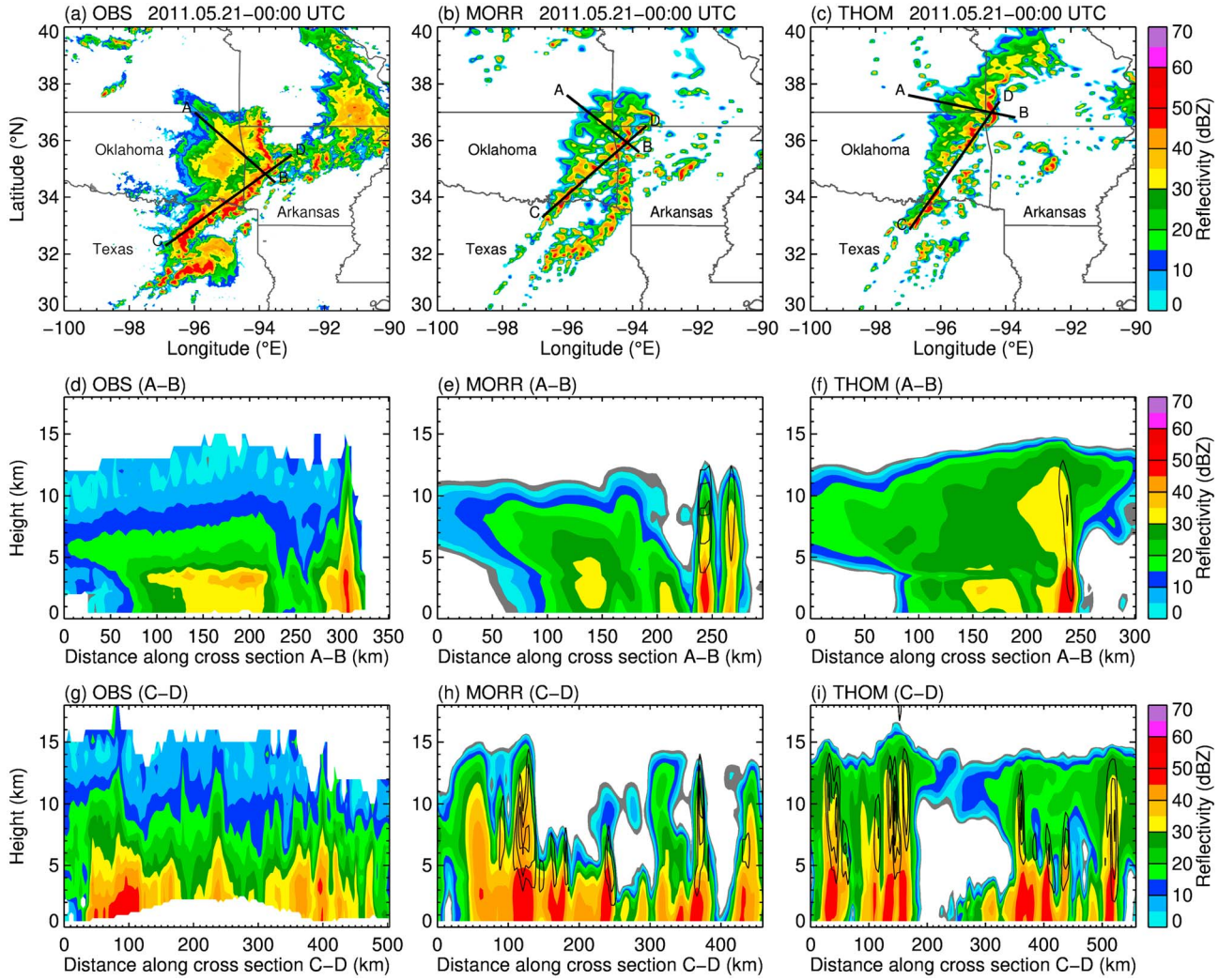

Figure 3. An example of an intense mesoscale convective system from (left) Next-Generation Radar 3-D mosaic radar observations and (middle) model simulation with Morrison microphysics and (right) Thompson microphysics. (a–c) Horizontal radar reflectivity at 2.5 km height, (d–f) vertical cross sections along the line (A-B) perpendicular to the convective line in (a–c), and (g–i) vertical cross sections along the line (C-D) parallel to the convective line in (a–c). The black contours in (e) and (f) and (h) and (i) are simulated vertical velocities in 5 m s^{-1} interval.

Vertical cross sections show (Figures 3d and 3g) 10-dBZ echo-top within the leading convective line reaching to 14 km height, with intense 40-dBZ echoes (likely containing graupel or hail particles) reaching 6–7 km. Both WRF simulations produced an MCS with a smaller stratiform precipitation area and less coherent intense convective line compared to those observed. Vertical cross sections of the model simulated reflectivity (Figures 3e, 3f, 3h, and 3i) show intense echoes associated with strong updrafts (black contours) reaching similar altitudes across the convective line. The free-running regional climate simulations in this study were designed to examine the statistics of MCS properties, rather than representing specific events. Therefore, we do not expect the model to reproduce the exact timing, location, and evolution of individual MCSs. This example shows that the 4-km WRF model is able to produce certain radar observed MCS features including the vertical structures. We will examine the simulated MCS properties in more detail in section 4.

3.3. Identifying Robust MCSs and Life Cycle Stages

With the satellite tracked T_b data that identify potential MCSs, we define robust MCSs (RMCSs) using the storm structure characterized by radar reflectivity data. The method is similar to that of Coniglio et al. (2010). A CCS-identified MCS, as described in section 3.1, is defined as a RMCS if (1) the PF major axis

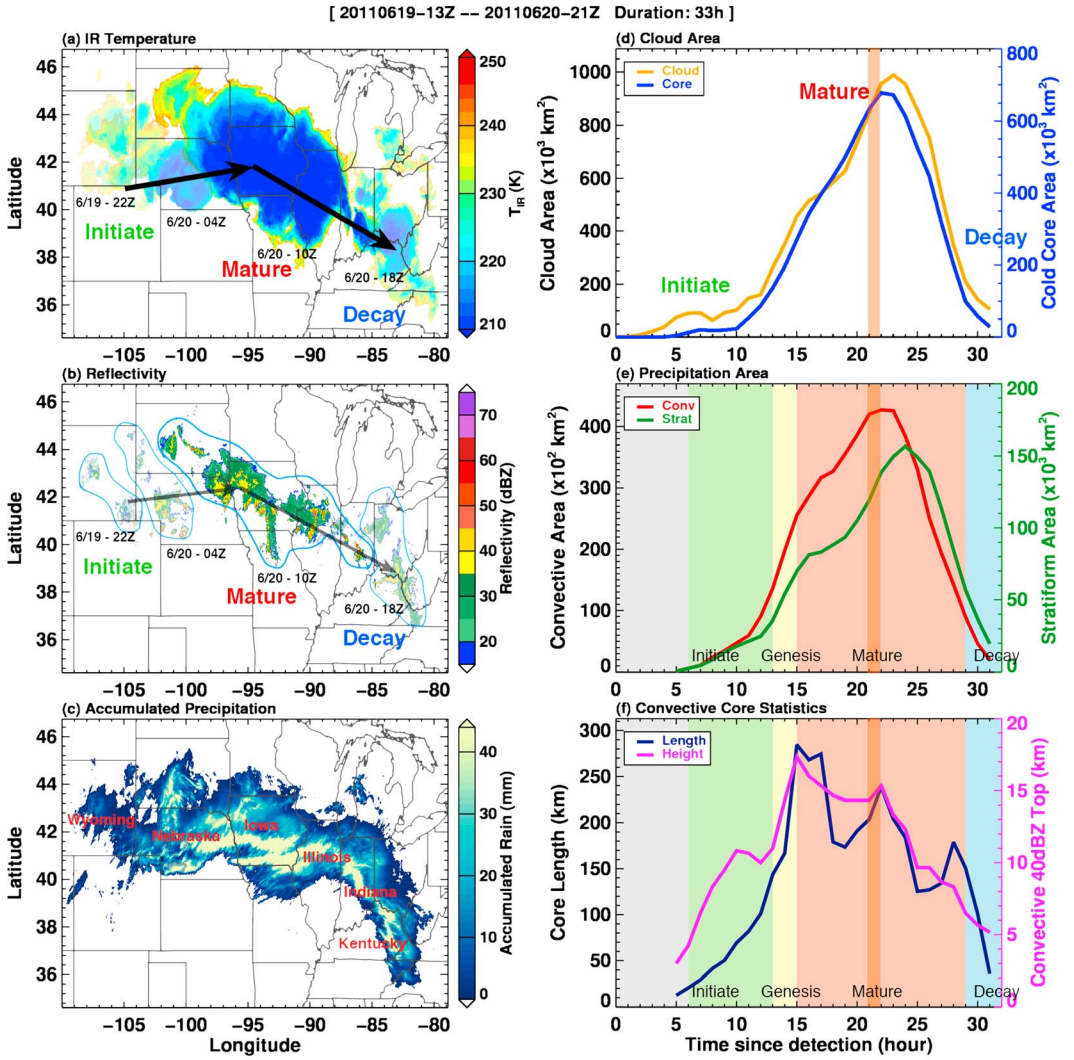

Figure 4. Example of an observed robust mesoscale convective system (MCS) identified and tracked by the tracking algorithm. (a) Snapshots of cloud top brightness temperature at various times. (b) Snapshots of radar reflectivity at 2.5 km height at various times; the blue lines outline the approximate location of the convection. (c) Accumulated precipitation over the lifetime of the MCS. (d) Time series of cloud shield area evolution. (e) Time series of precipitation area evolution. (f) Time series of largest convective core length and maximum 40-dBZ echo-top height evolution. The color shadings in (e) and (f) show objective life cycle stage definition. The orange vertical bar in (d)–(f) marks the mature MCS stage (20 June 2011 at 10 UTC) in (a) and (b).

length exceeds 100 km and (2) the PF contains some embedded echoes ≥50 dBZ for at least 5 continuous hours (Figure 2b). This definition is also consistent with the MCS definition of Yuan and Houze (2010) except that using orbiting satellite data, they could not determine the time scale. Our definition eliminates convective storms that have not achieved a mesoscale horizontal extent and those that do not contain persistent intense convection, or some persistent high cloud shields that are associated with a large synoptic disturbance but contain negligible precipitation. Figure 4 shows an example of a RMCS identified by FLEXTRKR. This MCS lasted 33 hr and propagated across six states in the Midwest area, producing large areas of heavy precipitation (Figures 4b and 4c). Time series of the sizes of CCS cloud-shield and convective/stratiform precipitation are shown in Figures 4d and 4e. During the mature stage of the MCS, the combined convective/stratiform precipitation area (~200,000 km^2) is 33% larger than the state of Illinois. This long-lasting MCS produced widespread heavy precipitation in a 2,500-km long swath during its lifetime.

Each RMCS is objectively categorized into four lifecycle stages using a method modified from the subjective definition by Coniglio et al. (2010): (1) convective initiation, (2) genesis, (3) mature, and (4) decay. The convective initiation stage is defined as the time period between the first occurrence of precipitating convective cells and before the genesis stage. The genesis stage occurs during the first hour after the major axis length of a convective cell/line exceeds 100 km. The mature stage is defined as the period when the convective cell/line maintains its major axis length of 100 km and the stratiform rain area is larger than the mean value during the entire length of the MCS. An MCS reaches its decay stage when the major axis length of the convective cell/line is less than 100 km or the stratiform area decreases to below the mean value after the mature stage. Figures 4e and 4f (color shading) show the four lifecycle stages defined for the MCS. The convective cell/line in this MCS showed upscale growth in cell size and deepening of echo-tops between 6 and 13 hr after detection of the CCS (Figure 4f). The convective cell/line major axis length eventually reached 100 km and rapidly transitioned into a mature MCS, when the large precipitation area had persisted for 14 hr. The period in which the core length drops below 100 km is labeled as decay and corresponds to the last 4 hr of the example in Figures 4e and 4f. This objective lifecycle stage categorization is used throughout this study to identify the genesis and mature stages of MCS, which are the periods of primary precipitation production.

4. Results

In this section, we compare MCS properties and associated precipitation statistics simulated by the WRF regional climate model against observations and examine the impact of microphysics parameterizations on the model representation of MCSs and their associated feedback to the large-scale environments.

4.1. Regional MCS Precipitation Statistics

MCS precipitation frequency, precipitation amount, and MCS fraction of total precipitation averaged from May through August 2011 are shown in Figure 5. Although the spatial patterns of simulated MCS precipitation frequency and amount are in general agreement with observations over a large area in the central United States, there are notable differences among the two simulations and the observations. The simulation with Morrison microphysics (MORR) has more frequent MCS precipitation and amount in the Northern Great Plains and southeastern central United States than the simulation with Thompson microphysics (THOM) and observations. The averaged biases of MCS frequencies in the central U.S. region (magenta box in Figure 5) are 20% and −10% for MORR and THOM, respectively. As a result, the averaged MCS precipitation biases are 13% (MORR) and −20% (THOM). The spatial patterns of total precipitation are quite similar to MCS precipitation except with larger magnitudes (Figure S1 in the supporting information). The low bias of MCS in THOM is larger in July–August than May–June (Figure S2). Similar summertime dry bias in CPM regional climate simulations using THOM microphysics were reported by Prein et al. (2017) and attributed to weaker large-scale forcing in the summer months. Such dry biases were noticeably smaller in our MORR simulation (Figures S2 and S3). The exact cause of the biases in late summer, such as land-atmosphere interactions or synoptic environments, should be investigated in future studies. The observed mean MCS fraction of total warm season rainfall is 46% in the central United States (Figure 5g); the simulated fraction of mean MCS to total rainfall is biased high in MORR (54%) and slightly biased low in THOM (43%; Figures 5g and 5h).

As discussed in section 1, the propagation and diurnal timing of precipitation in central United States are poorly simulated by most GCMs with parameterized convection. The WRF simulated diurnal cycle of MCS precipitation averaged during May to August 2011 is shown in Figure 6. Both simulations produce two preferred locations of MCS precipitation initiation at ~18 LT, one near the foothills of the Rocky Mountains (104°W) and another further east over the Great Plains (99°W). The simulated MCS precipitation propagates eastward and maximizes around midnight in the central United States and weakens/dissipates at ~06 LT on the next day as they propagate toward the Appalachians Mountains (85°W). The simulations are able to capture the large fractional contribution (approximately half) of propagating MCS to total precipitation (Figures 6e and 6f), although the MORR MCS precipitation amount and fraction are slightly higher than observations, while the THOM MCS precipitation amount and fraction are biased low.

Figure 7 shows the comparison of MCS and isolated (non-MCS) precipitation averaged between the longitude band of 103°W and 87°W. Total precipitation is simply the sum of MCS and isolated precipitation (not shown). Precipitation from isolated convection peaked around sunset (~18 LT) and precipitation from

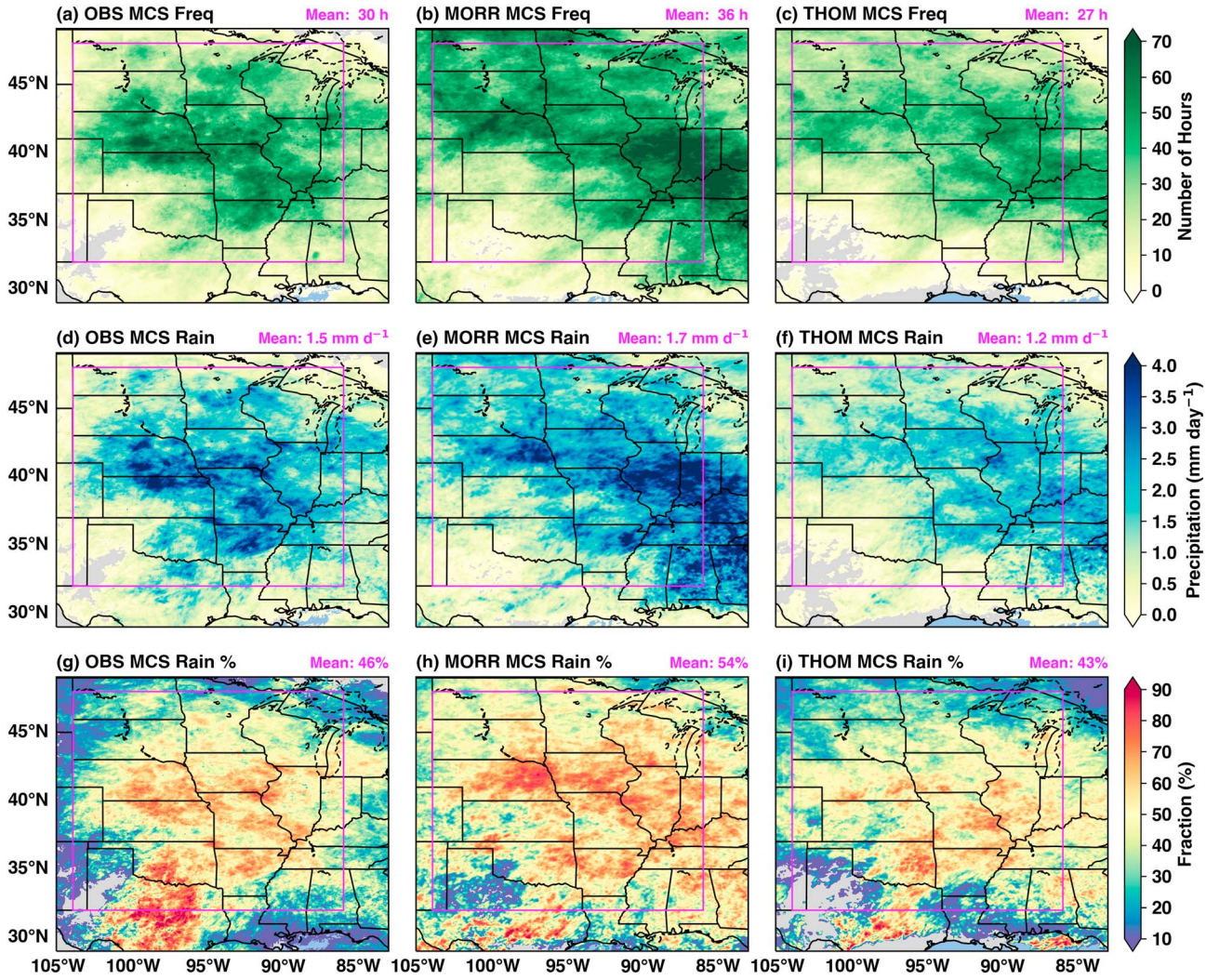

Figure 5. Warm season (May–August) mean mesoscale convective system (MCS) precipitation statistics over the central United States (a–c) MCS precipitation frequency, (d–f) MCS precipitation amount, and (g–i) MCS contribution to total precipitation. Average value within the magenta box is shown at upper right corner of each panel.

convection that grew upscale peaks 4–6 hr later, around midnight. MCS precipitation decays quickly after sunrise, and both types of precipitation have a minimum at local noon. It is clear that the nocturnal timing of peak precipitation is controlled by MCSs, and it is captured relatively well by the two simulations. MORR MCS precipitation between late afternoon and evening hours are biased high and peak about 2–3 hr earlier than observed. THOM MCS precipitation diurnal phase has good agreement with observations, but the average amount is biased low. The averaged MCS precipitation amount bias is 10% and −26% for MORR and THOM, respectively.

The ability of the two WRF CPM regional climate simulations in representing precipitation intensity and extremes at native model resolution (4 km) is shown in Figure 8. The frequency distribution of MCS and isolated (non-MCS) hourly precipitation is presented for four subregions: Northern Great Plains, Southern Great Plains, Midwest, and Southeast (shown in Figure 1). In observations, the frequency of intense precipitation (rain rate $>$ 20 mm hr^{-1}) from MCSs is significantly higher than that from isolated precipitation across all regions, consistent with previous studies on the importance of MCS in contributing to extreme precipitations (Stevenson & Schumacher, 2014). This contrast between the frequency of MCS and isolated rain rates is largely reproduced by the WRF simulations except for the low bias in THOM over the Southern Great Plains.

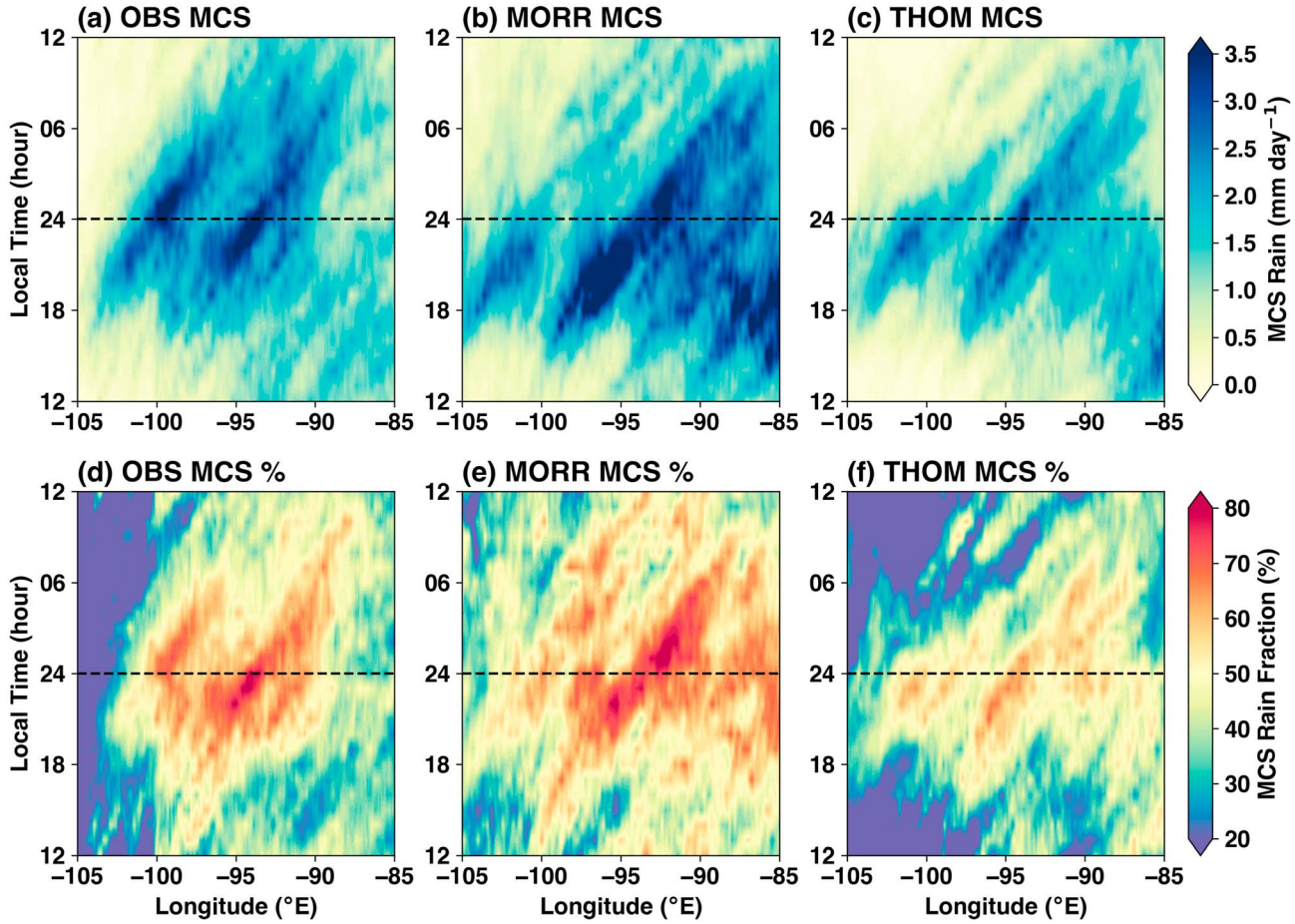

Figure 6. Warm season (May–August) mean diurnal cycle Hovmöller diagram of (top row) mesoscale convective system (MCS) precipitation and (bottom row) MCS contribution to total precipitation. (a and d) Observed precipitation, (b and e) Morrison microphysics, and (c and f) Thomson microphysics. Local time is set to North American Central Time Zone (UTC 06:00).

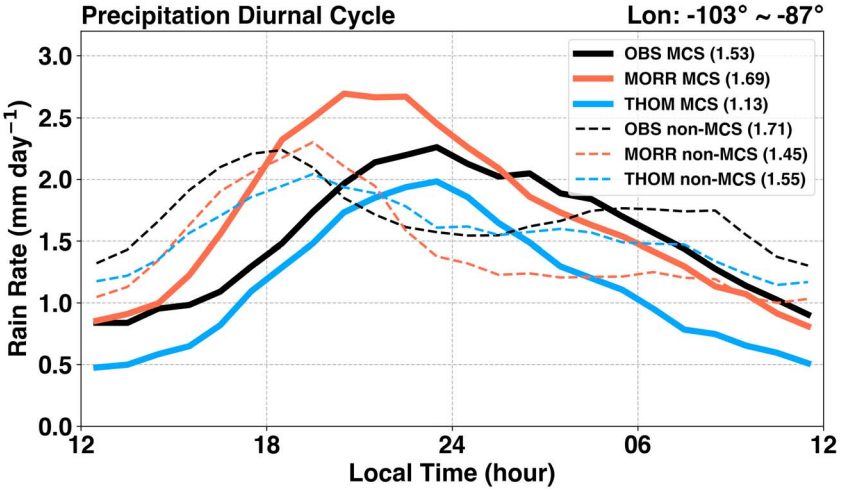

Figure 7. Warm season (May–August) mean diurnal cycle of precipitation averaged in central United States (103°W–87°W) from mesoscale convective system (MCS; solid lines) and non-MCS precipitation (dash lines). Mean values across the diurnal cycle are shown in the legend in units of mm d^{-1}. Local time is set to North American Central Time Zone (UTC-06:00).

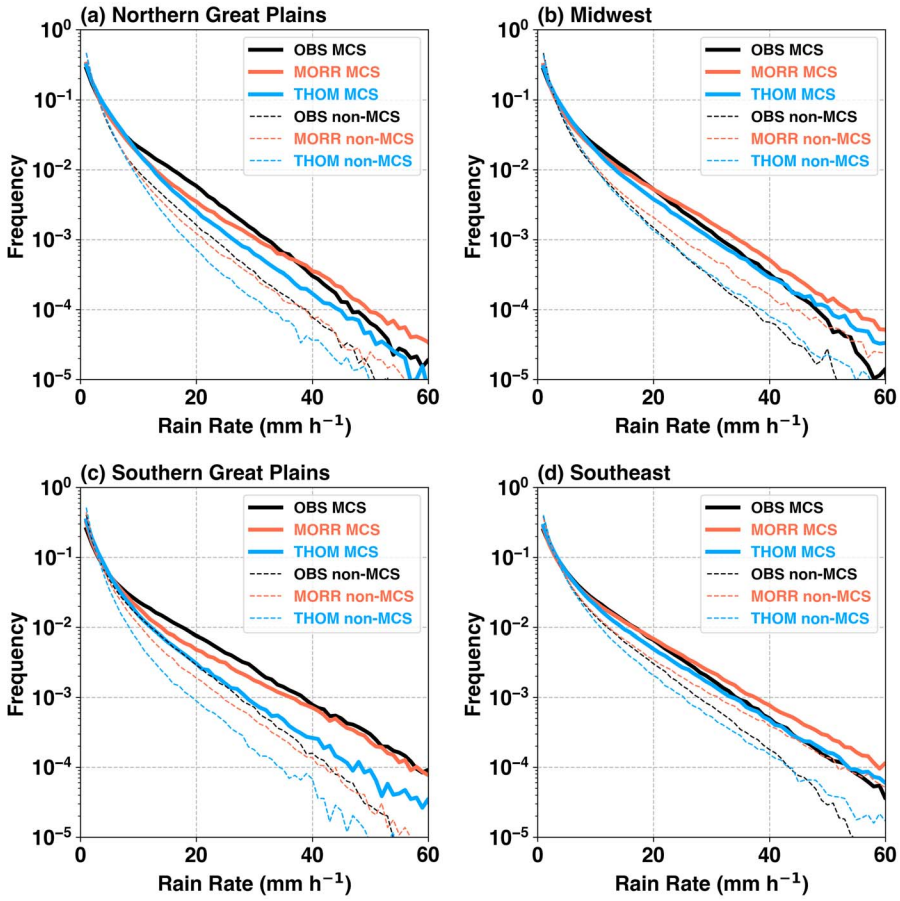

Figure 8. Frequency distribution of mesoscale convective system (MCS) and non-MCS hourly rain rate in 2011 for four sub-regions. (a) Northern Great Plains (40°N–48°N, 104°W–95°W), (b) Midwest (40°N–48°N, 95°W–86°W), (c) Southern Great Plains (32°N–40°N, 104°W–95°W), and (d) Southeast (32°N–40°N, 95°W–86°W). The four sub-regions are shown in Figure 1 (blue boxes).

4.2. Evaluation of MCS Characteristics

In this subsection, we evaluate the fidelity of the WRF CPM simulations in representing MCS characteristics observed by the NEXRAD radar network. In a free-running regional climate simulation with a large domain and constrained only by the lateral boundary conditions, the simulations are able to capture large-scale disturbances and associated major convective outbreaks in approximately similar timing and area of observed events. An example of precipitation Hovmöller diagram between observations and two simulations in June 2011 is shown in Figure S4. However, we do not expect the model to reproduce individual MCSs at the exact times and locations compared to observations. Instead, we focus on evaluating the composite of a population of MCS properties and sensitivities to microphysics parameterizations.

Figures 9a–9c show the tracks of individual MCS colored-coded by the amount of precipitation accumulated during the lifetime the MCS. The two WRF simulations are able to produce MCSs with a wide variety of precipitation intensity, and they generally propagate eastward, in qualitative agreement with observations. However, in the THOM simulation, MCSs were biased low in the Southern Great Plains, consistent with the mean dry bias (Figure 5f), and MCS hourly rain rate frequency was underestimated (Figure 8c) in that region. The MORR simulation shows more high precipitation MCSs passing over the Southeast region, corroborating the wet bias in that area (Figure 5e). Both simulations have more MCS initiation than observations west of 102°W. It is possible that the higher terrain height and less dense radar network in that region reduce detectability of early convective initiation in observations.

Figures 9d–9f show the spatial distribution of warm-season averaged MCS propagation speeds. The median propagation speed of each MCS was mapped onto the respective native 4-km grid of the simulations and

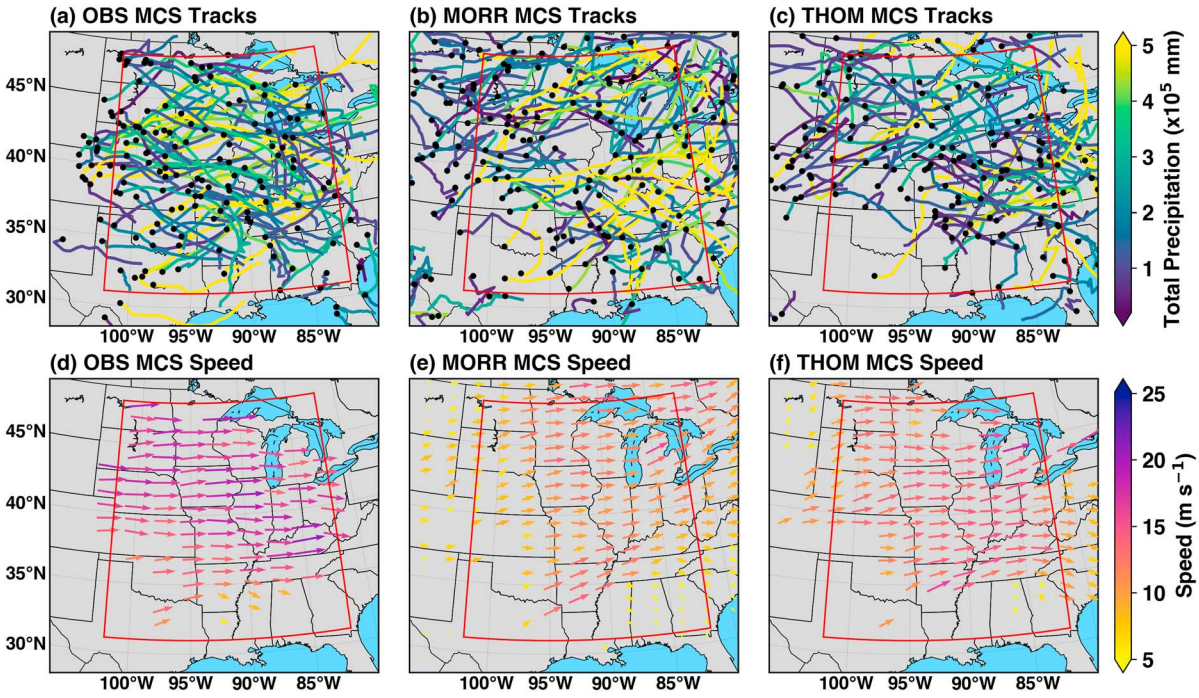

Figure 9. (a–c) Mesoscale convective system (MCS) tracks colored by total precipitation during their lifetime and (d–f) averaged MCS propagation speed. The black dots in (a)–(c) denote locations of MCS convective initiation detected by using low-level radar reflectivity data. Areas with less than 20 data samples were excluded in the propagation speed calculations.

observations and subsequently averaged across all MCSs during the warm season. Observed MCSs propagate predominantly eastward at a speed of 20–25 m s^{-1} north of 40°N. Perhaps related to the weaker ambient winds between 700 and 400 hPa (i.e., steering level winds, Carbone et al., 2002), MCSs south of 40°N tend to propagate at a slower speed $<$20 m s^{-1}. The north-south contrast in propagation speed is smaller in the model simulations. While the simulated MCS propagation speeds are in general agreement with observations in the south-central United States, both simulations underestimate the faster propagation speed in the northern region. In the subsequent sections, we limit our analysis to MCSs that spend more than half of their lifetime over the central U.S. region (red boxes in Figure 9, 102°W–82°W, 31°N–48°N), where the NEXRAD radar network coverage is densest (Figure 1b). A total of 127, 107, and 109 RMCS were identified in the observations and MORR and THOM simulations, respectively.

Comparisons of the MCS PF equivalent diameter ($D = 2\sqrt{\text{Area}/\pi}$.), convective cell/line aspect ratio, and propagation speed during the mature stage are presented in Figure 10. The simulated size of MCS PFs is underestimated by 26% (MORR) and 12% (THOM). This underestimation is mainly caused by inadequate simulation of stratiform rain (discussed next), which has important implications regarding how the simulated MCSs interact with their large-scale environments. Both simulations also underestimate the maximum aspect ratio of the convective cell/lines by 26% (MORR) and 24% (THOM). Given the definition of RMCSs that require a convective cell/line major axis length maintaining above 100 km during the mature stage, this bias in convective cell/line aspect ratio suggests that the simulations underestimate the observed frequency of MCSs that contain an elongated convective line.

Comparisons of the MCS propagation speed show that a majority of the observed RMCSs in this study have propagation speed between 5 and 25 m s^{-1}, with a mode of ~20 m s^{-1}, consistent with earlier studies (Carbone et al., 2002; Corfidi et al., 1996). Both simulations underestimate the average propagation speed by 28% (MORR) and 23% (THOM), as the frequency of faster moving MCSs ($>$20 m $^{-1}$) that typically occur in the northern part of central United States is significantly underestimated (Figures 9d–9f). Comparisons of mean wind speeds at the steering level (700 to 400 hPa, Carbone et al., 2002) between the simulations and North American Regional Reanalysis (Mesinger et al., 2006) reveal that the model large-scale winds do not have significant biases (not shown). The simulated MCS propagation speed biases are possibly related

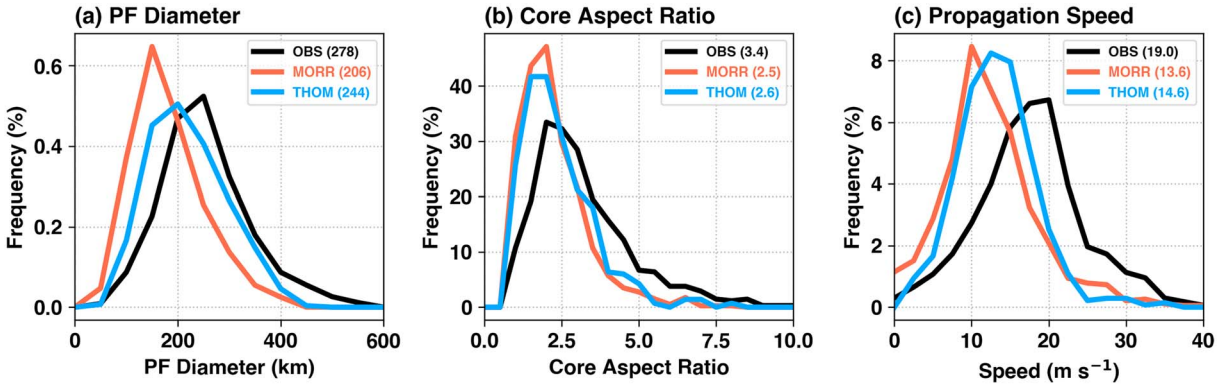

Figure 10. Frequency distribution of mesoscale convective system (a) precipitation feature equivalent diameter, (b) convective core aspect ratio, and (c) propagation speed during the mature stages. Mean values are provided in the legends.

to mesoscale and microphysical processes and will be further discussed in section 4.3. Clark et al. (2014) tracked individual PFs in weather forecasting WRF simulations using several microphysics schemes, including earlier versions of the MORR and THOM schemes used in this study. They found that all simulations overpredict the number of PFs, while they underestimate the propagation speed compared to observed PFs, with the THOM bias most pronounced in both aspects. The difference with our results could be caused by a number of factors, including the different types of simulations, and the tracking methodology difference. Propagation speeds in this study is estimated by the number of pixels advected that results in maximum 2-D correlation map of the MCS low-level reflectivity fields between two time steps (section 3.2), while in Clark et al. (2014), a simpler geographic center location difference of PFs between two time steps was used. Nevertheless, these low propagation speed biases have implications on the flooding potential simulated by CPMs. If the model adequately represents MCS rainfall intensity (Figure 8), a slower propagation speed may result in more rainfall accumulation at a given location and hence more conducive to flooding than in reality. Further investigation of the cause of the various biases and possible relationships among the biases and large-scale forcing conditions (Corfidi et al., 1996) and dependence on seasons (Carbone et al., 2002) is needed in future studies.

Finally, we examine the model simulated composite evolution of MCS cloud and precipitation structures (Figure 11). MCS lifetimes are normalized between 0 and 1, where 0 denotes convective initiation and 1 denotes dissipation. In this way, properties of MCSs with different lifetimes and the relative lifecycle stages can be composited to facilitate comparison. Both the CCS area and PF area show a steady increase from convective initiation during roughly the first half of the MCSs' lifetime (Figures 11a and 11b). The mature stage occurs between 50% and 70% of the MCSs' lifetime where the CCS and PF areas maximize and remain relatively stable before rapid dissipation. Significant differences between the two simulations are seen in the composite cloud and precipitation area. On average, MORR overestimated the CCS area by 61% and underestimated the PF area by 43%. In contrast, the THOM CCS area agrees quite well with observations (3% bias), while the PF area is underestimated by a smaller amount (26% bias).

One of the advantages of using a 3-D mosaic NEXRAD data set over a large region in this study is the ability to better characterize the internal three-dimensional structures of MCSs throughout their lifecycles as they propagate across the central United States. As discussed in section 3.2, MCSs are partitioned into convective and stratiform portions using observed and simulated radar reflectivity structures. The largest convective cell within any given MCS (which usually has multiple convective cells) is used to represent the most prominent convective feature. The composite evolution of convective cell area and maximum 40-dBZ echo-top height are shown in Figures 11c and 11d. The MORR convective cells are 56% larger and 14% shallower than observations. On the other hand, THOM produces much better agreement in both the mean (4% bias in area and −8% bias in echo-top heights) and temporal evolution. Our results suggest that large ice particles (hail/graupel, corresponding to high reflectivity such as 40-dBZ echoes) being lofted to the upper troposphere by strong convective updrafts occur less frequently than observed in both simulations. The impact of these biases on the microphysical processes and resulting surface precipitation will be discussed next.

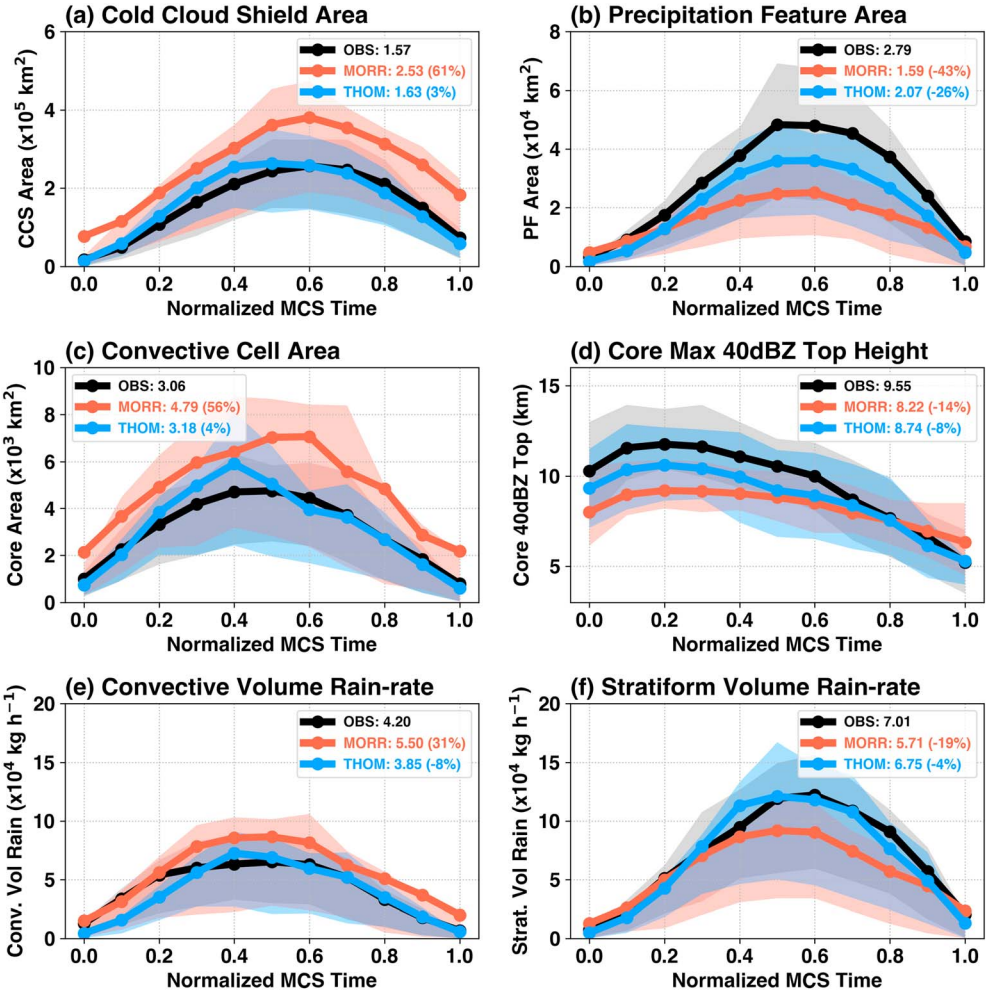

Figure 11. Composite evolution of mesoscale convective systems (MCSs). (a) Cold cloud shield area, (b) largest precipitation feature area, (c) largest convective cell area, (d) maximum 40-dBZ echo-top height in the largest convective cell, (e) convective volumetric rain rate, and (f) stratiform volumetric rain rate. MCS lifetimes are normalized between 0 and 1, where 0 denotes convective initiation and 1 denotes dissipation. The thick lines with filled circles are mean values, while the shaded areas show the interquartile range. The numbers in the legends are averages throughout the lifecycle, and the values in parentheses are mean biases from the simulations compared to observations.

Figures 11e and 11f depict the convective and stratiform volumetric rain rate, defined as

$$V_{\text{rainrate}} = \overline{\text{rainrate}} \times \text{area} \times \rho$$

where $\overline{\text{rainrate}}$ is the areal mean rain rate and ρ is the density of water. Convective volume rain rates increase rapidly in the first 1/3 of the MCSs' lifecycle and reach maxima just before halfway into the lifetime. High convective rain rates lead the peak stratiform rain rates by about 20% of the MCSs' lifetime. Again, significant differences between two microphysics schemes are evident. MORR overpredicts convective volume rain rates by 31% and underpredicts stratiform rain rates by 19%, while THOM has smaller biases compared to observations (−8% convective and −4% stratiform). Biases in the MORR convective volume rain rate are mainly caused by larger convective cell area, while in THOM, convective area and areal mean rain rate are both biased low (not shown). Stratiform volume rain rate biases are a result of compensating errors between underestimated stratiform rain area (−46% MORR and −28% THOM) and overestimated stratiform areal mean rain rate (31% MORR and 20% THOM; Figure S5).

To better understand the differences in simulated MCS macrophysics properties between the two microphysics schemes, we examined several microphysical quantities from the two simulations. Figure 12 shows

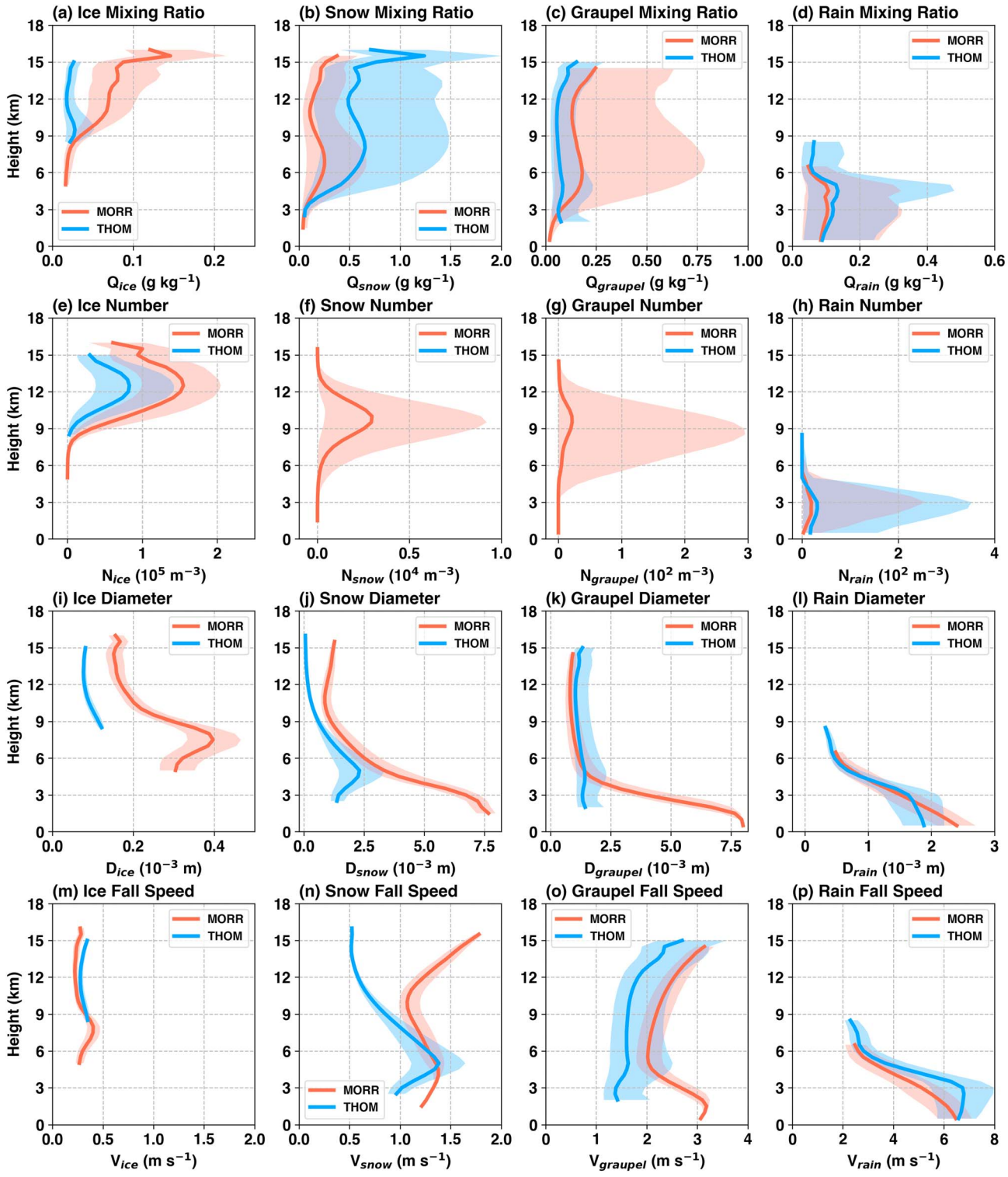

Figure 12. Composite profiles of (top row) mixing ratio, (second row) number concentration, (third row) mass-weighted mean diameter, and (bottom row) mass weighted mean fall speed for four hydrometeor species from the two simulations. They are (a, e, and i) cloud ice, (b, f, and j) snow, (c, g, and k) graupel, and (d, h, and i) rain. Only data within the tracked cold cloud shield of MCSs during the genesis and mature stages are included. The solid lines show the averaged of the median profiles, and the shadings denote averaged interquartile ranges. Note that snow and graupel in Thompson microphysics are single moment so their number concentration were omitted in (f) and (g). Averaged profiles with data samples $<5 \times 10^4$ at each height are excluded in the figure.

composites of mixing ratio, number concentration, mass-weighted mean diameter, and mass-weighted mean fall speed for cloud ice, snow, graupel, and rain within the same RMCSs analyzed in Figure 11. Details of calculating the microphysical quantities are provided in the Appendix in the Supporting Information. To obtain the composite profiles, the median and interquartile range of each microphysics quantity was first obtained within the cold cloud shield of each tracked RMCS at a given hourly snapshot; then the median and interquartile range profiles across over 100 RMCSs during each of their genesis and mature stages were further averaged. Therefore, a large number of data samples (typically on the order of $>10^6$ at each height for each species) were included in Figure 12 to ensure robustness of the results.

Substantial differences across the three ice phase hydrometeor species were observed. The mixing ratio and number concentration of small cloud ice particles is substantially higher in MORR than THOM in the upper troposphere (Figures 12a and 12e). These cloud ice particles have very small fall speeds (Figure 12m). The larger amount of cloud ice with slow fall speeds would lead to larger spread and slow dissipation of anvil clouds (Fan et al., 2013), which would contribute to the larger upper level MCS cold cloud shields in the MORR relative to THOM (Figure 11a). In contrast, snow mixing ratio in THOM is 2–3 times higher than MORR throughout much of the troposphere (Figure 12b). These abundant snow particles in THOM have smaller diameter (Figure 12j), and they generally fall slower than MORR throughout the troposphere except around the melting layer (Figure 12n). The more abundant and slower falling snow particles explain the larger stratiform rain area in the THOM simulation (Figure 11b). The difference in cloud ice and snow microphysics properties and resulting upper-level cloud macrophysics characteristics found in this study are consistent with simulation results of MCSs in Tropical Western Pacific reported by Van Weverberg et al. (2013). Powell et al. (2012) also showed higher ice mass in the upper tropospheric thin anvil clouds in MORR, while THOM has significantly larger ice mass in the midtropospheric thick anvils in MCS simulations over West Africa.

The MORR scheme produces significantly higher graupel mixing ratio than THOM, in contrast to snow particles (Figure 12c). Although graupel particles in MORR have slightly smaller diameters than THOM above the melting layer, they have faster fall speeds throughout the troposphere (Figure 12o). Since graupels are primarily produced in convective updrafts (Fan et al., 2017), they are generally associated with high radar reflectivity due to their high density and large size. Larger and slower falling graupel particles above 6 km in THOM are likely the cause for higher 40-dBZ echo-tops in the convective core regions compared to MORR shown in Figure 11d. Finally, rain mixing ratio, number concentration, and diameter have relatively smaller differences between the two simulations than ice hydrometeors (Figures 12d, 12h, and 12i). We note that below 3 km, THOM has slightly larger raindrop number concentrations and smaller diameter, suggesting that more raindrops are prone to evaporation than MORR below the stratiform cloud base, which could enhance downdrafts and support stronger cold pools in THOM. Although raindrop fall speeds are slightly higher in lower troposphere (<5 km) in THOM, they are comparable near the surface (Figure 12p). Similar raindrop mass, concentrations, and fall speeds near the surface suggest that their total surface precipitation is comparable. This is indeed the case where the total volume rain rates averaged for each RMCS between the two simulations differ by only 2% (Figure S6).

In summary, based on the various MCS cloud and precipitation property comparisons shown in Figure 11, we infer that in general, the THOM simulation produces better agreement with observations in upper-level cloud shield and precipitation area, convective feature horizontal and vertical extents, and partitioning of precipitation types. The MORR simulation detrains more smaller/slower-falling ice particles that stay lofted longer in the upper-level nonprecipitating anvil clouds, as opposed to the THOM simulation having more slow-falling snow particles that melt and produce stratiform precipitation. While both simulations underestimate stratiform rain area to different extent, consistent with previous studies, THOM produces volume convective and stratiform rainfall that are similar to observations. As discussed in the introduction, larger fraction of stratiform precipitation results in top-heavier diabatic heating profiles (Schumacher et al., 2004). Long-lived MCSs have been shown to enhance the middle-to-upper level diabatic heating as a result of more robust stratiform rain, which strengthens the mesoscale circulation of the MCS and in turn promotes longer lifetime of MCSs (Yang et al., 2017). Our results in this section show that THOM microphysics produces more stratiform precipitation, in better agreement with observations, than the MORR microphysics, which were used in Yang et al. (2017). More robust stratiform precipitation suggests that MCSs in the THOM simulation may have more top-heavy diabatic heating, which favors generation of a MCV (Houze, 2014, pp. 282–286) and associated positive feedback to the mesoscale environment. We will further examine these aspects next.

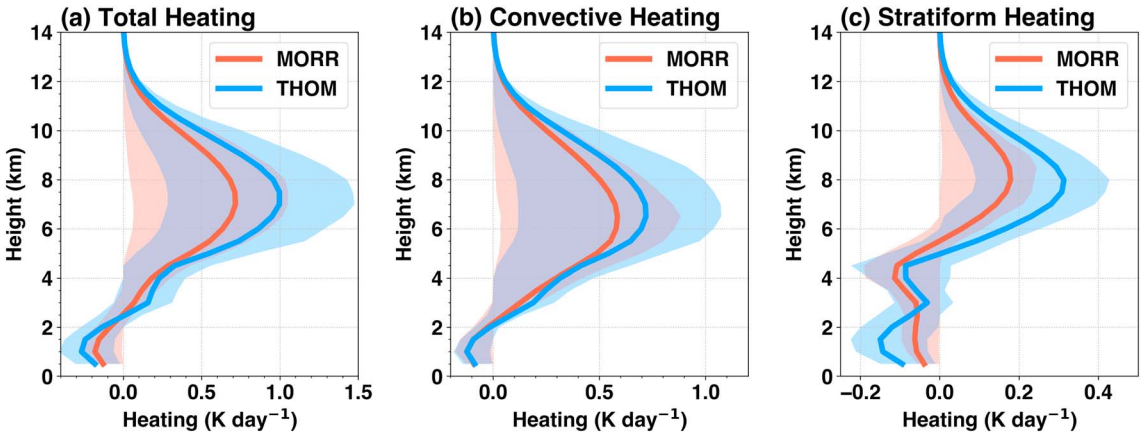

Figure 13. Average heating profiles for long-lived (15–30 hr) mesoscale convective systems. (a) Total heating, (b) convective heating, and (c) stratiform heating. The lines are mean values, and the shadings denote interquartile ranges.

4.3. Interactions and Feedbacks With Large-Scale Environments

To better understand the impact of microphysics parameterizations on the diabatic heating associated with MCSs, we isolated the heating profiles within the PFs of the simulated MCSs at any given instant and labeled them as "MCS heating profiles". Since Yang et al. (2017) showed that long-lived MCSs produce enough top-heavy heating to affect the synoptic-scale flow noticeably, we focus the present analysis on MCSs that last 15–30 hr over the central United States (Figure 1). All long-lived MCS heating profiles in the model simulation at a given time (heating outside MCSs) are set to zero to obtain "domain averaged MCS heating profiles." Totals of 56 and 72 long-lived MCSs were identified from the MORR and THOM simulations, respectively. To make a fair comparison, 56 MCSs were randomly selected from the THOM simulation for composites. Sensitivity test of randomly selecting 20 and 40 MCSs from both simulations does not change our findings. The selected domain averaged MCS heating profiles were further averaged throughout the entire warm season and shown in Figure 13.

Figure 13a shows that the total MCS diabatic heating profiles in the THOM simulation are more top-heavy than those in the MORR simulation. Although both heating profiles peak between 6 and 8 km, a stronger vertical gradient of heating profiles between 4 and 7 km is seen in the THOM simulation. To better explain the difference in the total heating profiles, they are further separated into convective and stratiform using the same method described in section 3.2. While the upper level convective heating is slightly stronger in the THOM simulation, the vertical gradients below the peak heating are similar (Figure 13b). In contrast, the THOM stratiform heating profiles are almost twice as strong at upper levels (~8 km) and have a sharper gradient between 4 and 7 km compared to MORR (Figure 13c). The stronger upper-level heating and lower-level cooling profiles from the THOM simulation are consistent with having more stratiform precipitation in THOM than in MORR (Figure 11f).

To examine the sensitivities of the environmental feedback from MCS heating to microphysics parameterizations, we follow the same relative MCS environmental composite analysis used by Yang et al. (2017). Meteorological variables centered at the geometric centroid of the MCS PF were composited over a moving box (350 × 200 grid points or ~13°longitude × 7°latitude). We included only the same long-lived MCSs used in the heating profile analysis. Anomalies of the meteorological variables were calculated by subtracting the grid mean values for the same hour and for each month to remove the mean diurnal and seasonal variations. Variables were composited on fixed pressure levels at 850, 700, 600, 500, 400, and 300 hPa. Since MCSs produce the majority of their precipitation, particularly stratiform precipitation, during their mature stages (Figure 11f), we composited their environment anomalies during the mature stage as defined in section 3.3.

Figure 14 shows the composite mesoscale environment anomalies during the mature MCS stages at three representative pressure levels between the two simulations. Consistent with many previous studies (e.g., Maddox, 1983), both simulations show MCSs commonly occurring ahead of a trough to the west. At

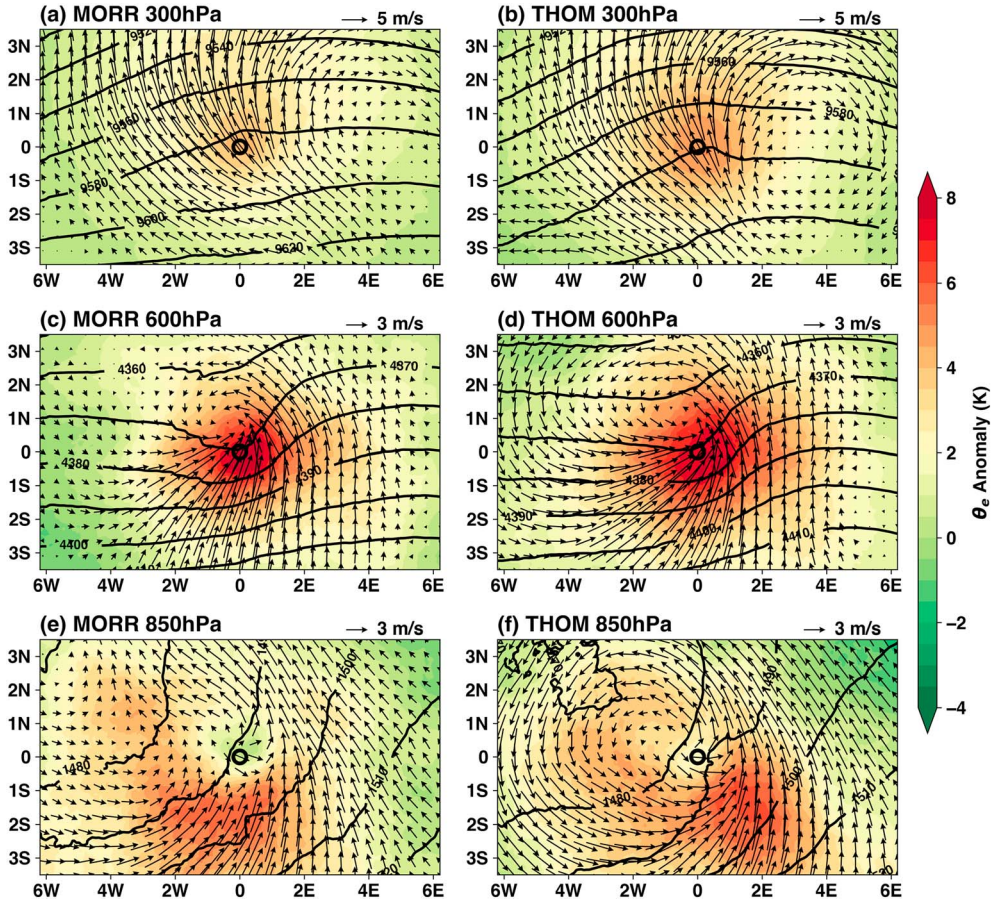

Figure 14. Relative-location composites of mean geopotential height (in meters, contour lines), anomaly wind (vector), and anomaly equivalent potential temperature ($\Delta\theta_e$, shaded) at (a and b) 300 hPa, (c and d) 600 hPa, and (e and f) 850 hPa during mature MCS stages for (left column) Morrison and (right column) Thompson microphysics. The *x* and *y* axes show relative distances away from the composite centers (mesoscale convective system precipitation feature geometric centers).

850 hPa (Figures 14e and 14f), strong southerly wind anomalies over a broad area just ahead of the eastward propagating MCS (Figures 9e and 9f) transport unstable high-θ_e air from the Gulf, consistent with the Great Plains low-level jet commonly observed in MCS environments (Coniglio et al., 2010). A cyclonic flow anomaly centered 2° west of the MCS centroid is more clearly seen in the THOM simulation, possibly a result of downward momentum transport from the wind flow above.

At 600 hPa (Figures 14c and 14d), a clear signature of a mesoscale vortex is seen in both simulations. However, the magnitude of the anomaly vortex is much stronger in the THOM simulation. Potential vorticity is generated in the layer of strong vertical heating gradients from the long-lived MCSs. When strong enough, such potential vorticity generation can manifest as a quasi-balanced vortex referred to as an MCV, which, in turn, sustains the systems via a "dynamical flywheel" to support vertical lifting on the periphery of the MCSs (Chen & Frank, 1993; Fritsch et al., 1994; Houze, 2014, pp. 284–286). More importantly, our results show that simulated MCSs with more realistic stratiform precipitation amount and top-heavier heating profiles (i.e., THOM) are clearly associated with a stronger MCV signature at midlevel. A stronger westerly flow component into the southwest side of the MCS centroid is seen with the well-defined MCV in THOM. Potential temperature anomaly composites show that the stronger westerlies ingest cooler air into the rear of the MCSs (not shown), which enhances the rear-to-front sloping of the mesoscale downdraft (Houze et al., 1989) and thus helps to maintain the eastward propagation of the MCS. Stronger midlevel rear inflow of dry air into the MCSs, along with potentially stronger evaporation that supports downdraft induced cold pools as suggested by more numerous and smaller raindrops (Figures 12h and 12l), are consistent with faster MCS propagation speeds in THOM (Figure 10). Since the averaged total volumetric rainfall is similar between the two

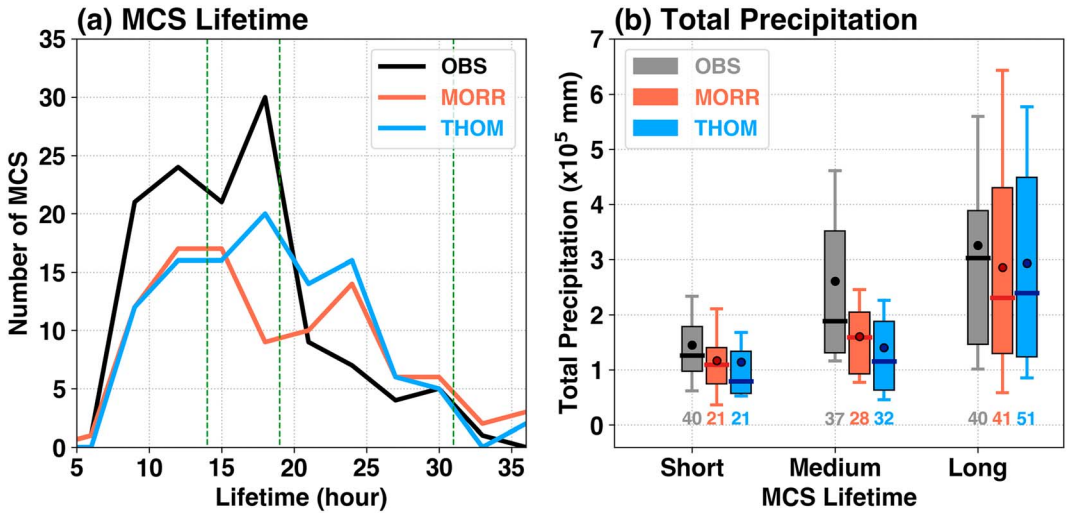

Figure 15. (a) Distribution of mesoscale convective system (MCS) lifetime and (b) total MCS precipitation segregated by three lifetime groups, shown between the green dash lines in (a). Total MCS precipitation is calculated by summing all precipitation during the lifetime of each MCS. In (b), the horizontal bars are medium values, the circles are mean values, the boxes show the interquartile range, and the whiskers denote 10th and 90th percentile values. The numbers below the bars in (b) are number of MCSs in each group.

simulations (Figure S6), the slower propagation speed in MORR may be partially responsible for larger precipitation amount in a given region (Figure 5).

At upper levels (e.g., 300 hPa), a ridging in geopotential height and mesoscale divergent wind field are seen around the MCS centroid and further to the north (Figures 14a and 14b). The anticyclonic flow anomaly east of the MCS and the divergent wind anomaly appear slightly stronger in the THOM simulation compared to that in MORR. Such an upper-level divergent field is a further signature of long-lived MCSs in the THOM simulation.

These analyses suggest that use of the THOM microphysics scheme leads to a stronger positive mesoscale dynamical feedback favoring generation of new convection at the periphery of the MCV and promoting eastward propagation of the MCS. The latter is consistent with the slightly higher propagation speed simulated by THOM than MORR (Figure 10c). The mesoscale anomaly seen in the THOM simulation indicates that the MCSs in that case are more self-sustaining and thus have a greater net effect on the large-scale environment. The comparison of the distribution of MCS lifetimes shown in Figure 15a supports this inference. While both simulations underestimate the observed number of MCSs lasting between 8 and 18 hr, there are more MCSs lasting between 15 and 25 hr in THOM than in MORR.

Although the number of very long-lived MCSs (>20 hr) is considerably smaller than the number of shorter-lived ones in observations, the long-lived MCSs contribute disproportionately to precipitation. Figure 15b shows the distribution of total precipitation accumulation per MCS from short ($t < 14$ hr), medium ($14 \text{ hr} \leq t < 19$ hr), and long-lived ($t \geq 19$ hr) MCSs. It is clear that medium- to long-lived MCSs (≥14 hr) can produce two to three times the amount of precipitation compared to short-lived ones. We note that the simulated distribution of the long-lived MCS total precipitation agrees better with observations than the medium- and short-lived ones. Since the averaged total MCS volume rainfall is comparable between the two simulations and observations as discussed in section 4.2, the long-lived MCSs in the simulations possibly compensated for the low precipitation biases from the shorter-lasting ones.

While the Great Plains low-level jet has important influence on the development and evolution of MCSs in the central United States (e.g., Yang et al., 2017), we did not find noticeable difference in its strength between the two simulations partly because the Great Plains low-level jet is strongly influenced by the large-scale horizontal pressure gradient over the sloping terrain of the Great Plains, which is constrained by the prescribed lateral boundary condition. In global climate simulations, however, uncertainty in cloud microphysics parameterizations could potentially influence the low-level jet, making it harder to disentangle the various effects cloud microphysics parameterizations can have on MCS simulations.

5. Conclusions

Two sets of regional climate simulations over the contiguous United States during the boreal warm season (May–August) of 2011 were conducted using WRF CPM at 4-km grid spacing with two commonly used microphysics parameterizations. Sensitivities of the simulated MCS properties and feedbacks to large-scale environments in the central United States were systematically examined. Our main goal was to elucidate differences in macrophysical characteristics of MCS that result from uncertainty in cloud microphysical parameterizations and to demonstrate some linkages between the MCS characteristics and the feedback from MCSs to the large-scale circulation that have important implications for climate modeling. We used two high-resolution observational data sets, including a geostationary infrared brightness temperature data set and a 3-D NEXRAD mosaic reflectivity data set, to assess the fidelity of model simulated MCSs. An objective tracking algorithm referred to as FLEXible object TRacKeR (FLEXTRKR) was applied to observations and model simulations to identify RMCSs over the central United States to facilitate comparison.

Similar to Prein et al. (2017) who analyzed MCS precipitation in a 13-year WRF convection permitting climate simulation, we find that the simulated warm season mean patterns of MCS precipitation frequency and amount are in general agreement with observations (Figure 5). MCSs contribute to approximately half of the warm season total precipitation in both simulations. This behavior is captured by the model simulations. Unlike Prein et al. (2017), however, simulations using two cloud microphysics parameterizations revealed notable uncertainty in the MCS simulations. More specifically, the averaged model MCS precipitation over the central United States is biased somewhat high in MORR (13%) and low in THOM (−20%). The diurnal cycle and propagation of MCS precipitation entities are well captured by the model (Figure 6). MCSs dominate the nocturnal peak precipitation, as a result of upscale growth from isolated precipitation that peak around local sunset (Figure 7). In addition to mean precipitation, the distribution of observed hourly MCS precipitation intensity is reproduced by the simulations (Figure 8). Intense MCS precipitation (rain rate $>$ 20 mm hr^{-1}) occurs significantly more frequently than non-MCS precipitation in both observations and simulations, indicating the ability of the CPM to simulate frequency of extreme rainfall associated with MCSs. These results demonstrate the advantage of CPM in simulating MCSs in a regional climate modeling framework compared to traditional coarse resolution climate models, suggesting that simulations from CPM could be used as benchmarks for future development of GCMs as they continue to increase in resolution and complexity of physics parameterizations.

Despite the success in representing regional MCS precipitation variability, differences exist in almost all MCS properties between the two simulations with different microphysics parameterizations. Importantly, 3-D NEXRAD radar data allow better characterization of MCS internal structures throughout their lifecycles that cannot be investigated using precipitation alone as in Prein et al. (2017) but are important for understanding the role of MCSs in the climate system. In general, the THOM simulation produces better agreement with observations in MCS upper-level cloud shield and precipitation area, convective feature horizontal and vertical extents, and partitioning of precipitation types (Figure 11). The MORR simulation generates more detrained small cloud ice particles that stay lofted as upper-level nonprecipitating anvil clouds, while the THOM simulation has more abundant slower falling snow particles (Figure 12) that melt and produce larger stratiform rain area and associated precipitation. Both simulations underestimate stratiform rain area to different extent, a common problem found in most microphysics parameterizations (Fan et al., 2017). The THOM simulation produces more stratiform volume rainfall that agrees better with observations than MORR. As a result, the MCS heating profiles in THOM are top heavier than MORR, such that they have a stronger vertical heating gradient in the midtroposphere (Figure 13). This difference represents a significant uncertainty in climate simulations using CPMs because the uncertainty has important implications for the macrophysical properties of MCSs that would ultimately lead to uncertainty in simulating the impacts of MCSs on the hydrological cycle and the large-scale circulation.

Analysis of multiple aspects of MCSs including their 3-D structure and diabatic heating confirmed that different treatments of cloud microphysics not only affect the simulated MCS properties but also have significant impact on their interactions to large-scale environments that ultimately provide feedbacks to the MCSs themselves. The stronger vertical heating gradients in THOM resulted in a stronger potential vorticity generation, often manifested as an MCV anomaly in the midtroposphere (Figure 14). This MCV anomaly helps to deepen the synoptic-scale trough with which the MCS is associated. In addition, it provides stronger westerly cool

and dry air advection into the MCS, which enhances the downward sloping rear-to-front flow (Smull & Houze, 1987) and helps to promote eastward propagation of the MCS. Such a positive mesoscale dynamical feedback favors prolonging the lifetime of MCSs, which in turn prolongs the MCS feedback to the larger scale. The longer-lived MCSs in the THOM simulation compared to the MORR simulation (Figure 15) thus have stronger upscale effects.

Based on comparison of the PDFs of observed and simulated MCS macroscale properties, we see relatively small differences between the THOM and MORR simulations in terms of the convective core aspect ratio but larger differences in the PF size, lifetime, and propagation speed. These results suggest that the similar biases in convective core aspect ratio in both simulations might be a result of biases in the simulated large-scale environment such as the background wind shear, which are unrelated to microphysical parameterizations. However, the notable differences between the two simulations suggest that cloud microphysical parameterizations have important effects on those MCS characteristics. Our analyses of the diabatic heating profiles and MCVs have provided an insightful explanation of the MCS lifetime differences. The greater frequency of rapidly propagating MCSs in the THOM simulations, compared to the MORR simulations, is consistent with the difference in advection of cool, dry air into the western sides of the MCSs by MCVs, which influences the balance between the effects of wind shear and cold pool on MCS maintenance. Sensitivity of squall line simulations to cloud microphysics and aerosols through changes in the cold pool has been noted in previous studies (e.g., Khain et al., 2009; Li et al., 2009). However, the substantial role of cloud microphysics in the strength of the MCVs that influence the cold pool as elucidated in this study has not been noted previously.

In summary, different treatment of cloud microphysical processes not only alters MCSs' convective-scale dynamics, as noted in many previous studies, but also has significant impacts on the macrophysical cloud properties such as lifetime and precipitation. Because long-lived MCSs produce 2–3 times the amount of rainfall compared to short-lived ones, treatments of cloud microphysics parameterizations will have a profound impact on simulating the hydrological cycle and extreme precipitation events in the climate system. Future efforts in improvements of the cloud microphysics parameterizations in convection and understanding of the interactions and feedbacks between MCS and large-scale environments would continue to be an important research topic in better understanding and projecting the impact of global warming on changes in hydrological extremes associated with MCSs.

Appendix A: The Calculation of Microphysical Variables

The gamma size distribution of hydrometeors assumed in MORR and THOM is expressed as

$$N(D) = N_0 D^{\mu} e^{-\lambda D}, \tag{A1}$$

where D is the particle diameter, N_0 is the intercept parameter, μ is the shape factor, and λ is the slope parameter.

The mass-weighted mean diameter (D_m) is defined as the fourth moment divided by the third moment of PSD:

$$D_m = \frac{\int_0^{\infty} D^4 N(D) dD}{\int_0^{\infty} D^3 N(D) dD}, \tag{A2}$$

where $N(D)\,dD$ is the number concentration between particle size D and $D + dD$. With the gamma distribution assumed in MORR and THOM, ((A2)) is then simplified as

$D_m=(4 + \mu)/\lambda$, (A3)where the slope parameter λ can be calculated from mixing ratio Q and number concentration N for the two-moment representation of hydrometeor, or the mixing ratio Q and the intercept parameter N_0 for one-moment representation of hydrometeor. Only data points with $Q > 10^{-5}$ kg kg^{-1} were included in the calculations. Since snow in THOM assumes a combination of two gamma distributions and its mass is proportional to D^2, the mass-weighted mean diameter for snow in THOM is calculated by the third moment of PSD divided by its second moment, which follows the code in the THOM scheme.

Mass-weighted mean fall speed is calculated as

Table A1
MORR

Species	Prognostic variables	ρ (kg m^{-3})	μ	a	b	c	d
Rain	Q_r, N_r	997	0	$\frac{\pi\rho_w}{6}$	3	841.9	0.8
Cloud ice	Q_i, N_i	500	0	$\frac{\pi\rho_i}{6}$	3	700	1
Graupel	Q_g, N_g	400	0	$\frac{\pi\rho_g}{6}$	3	19.3	0.37
Snow	Q_s, N_s	100	0	$\frac{\pi\rho_s}{6}$	3	11.72	0.41

Table A2
THOM

Species	Prognostic variables	ρ (kg m^{-3})	μ	a	b	c	d	f
Rain	Q_r, N_r	1,000	0	$\frac{\pi\rho_w}{6}$	3	4854	1	195
Cloud ice	Q_i, N_i	890	0	$\frac{\pi\rho_i}{6}$	3	1847.5	1	0
Graupel	Q_g	500	0	$\frac{\pi\rho_g}{6}$	3	442	0.89	0
Snow	Q_s	$\frac{6a_s}{\pi}D^{b_s-3}$	0.6357	0.069	2	40	0.55	100

$$V_m = \frac{\int_0^\infty V(D)m(D)N(D)dD}{\int_0^\infty m(D)N(D)dD}, \tag{A4}$$

where $V(D)$ is the particle fall speed-size relationship considering the air density adjustment. $m(D)$ is the mass-size relationship: $m(D) = a\,D^b$. Specifically, MORR assumes the particle fall speed-size relationship as $V(D) = (\rho_0/\rho)^{0.54}\,c\,D^d$, and THOM assumes the particle fall speed-size relationship as $V(D) = (\rho_0/\rho)^{0.5}\,c\,D^d \exp(-f\,D)$. The parameter ρ is the air density and ρ_0 is the constant air density at the reference level. The parameter ρ_0 is set to 1.0837 kg m^{-3} in MORR and 1.1845 kg m^{-3} in THOM.

The parameter values used in calculation is list in Tables A1 and A2. The detailed description of the references for the values in the tables can be found in Morrison et al. (2005), Morrison et al. (2009), Thompson et al. (2004), and Thompson et al. (2008).

Acknowledgments
The global merged satellite infrared data set was obtained from NASA Goddard Space Flight Center at the time of the study. The data set has since been migrated and can be accessed at the Goddard Earth Sciences Data and Information Service Center (https://disc.gsfc.nasa.gov/datasets/GPM_MERGIR_V1/summary?keywords=GPM_MERGIR_1). The NMQ mosaic NEXRAD 3-D reflectivity and Q2 precipitation data set was produced by the National Severe Storm Laboratory and obtained through Xiquan Dong at the University of Arizona. All raw model simulation and observation data were archived at the National Energy Research Scientific Computing Center (NERSC) High Performance Storage System (HPSS): /home/f/feng045/USA/Feng2018JAMES/. The final processed data used to generate the figures in the study can be accessed at https://doi.org/10.5281/zenodo.1186350. This study is mainly supported by the U.S. Department of Energy Office of Science Biological and Environmental Research (BER) as part of the Regional and Global Climate Modeling program through the Water Cycle and Climate Extremes Modeling (WACCEM) scientific focus area. Professor Houze's University of Washington participation is supported by the Pacific Northwest National Laboratory under Task Order 292896 (WACCEM) of Master Agreement 243766. Some developments of MCS tracking and observational data sets are also supported by BER through a Climate Model Development and Validation project. This research used computational resources from the National Energy Research Scientific Computing Center (NERSC), a DOE User Facility supported by the Office of Science under contract DE-AC02-05CH11231. PNNL is operated for DOE by Battelle Memorial Institute under contract DE-AC05-76RL01830.

References

Ban, N., Schmidli, J., & Schär, C. (2014). Evaluation of the convection-resolving regional climate modeling approach in decade-long simulations. *Journal of Geophysical Research: Atmospheres*, *119*, 7889–7907. https://doi.org/10.1002/2014JD021478

Beljaars, A. C. M. (1995). The parametrization of surface fluxes in large-scale models under free convection. *Quarterly Journal of the Royal Meteorological Society*, *121*(522), 255–270. https://doi.org/10.1002/qj.49712152203

Bentley, M. L., & Mote, T. L. (1998). A climatology of derecho-producing mesoscale convective systems in the central and eastern United States, 1986–95. Part I: Temporal and spatial distribution. *Bulletin of the American Meteorological Society*, *79*(11), 2527–2540. https://doi.org/10.1175/1520-0477(1998)0792.0.CO;2

Bentley, M. L., & Sparks, J. A. (2003). A 15 yr climatology of derecho-producing mesoscale convective systems over the central and eastern United States. *Climate Research*, *24*(2), 129–139. https://doi.org/10.3354/cr024129

Bryan, G. H., & Morrison, H. (2012). Sensitivity of a simulated squall line to horizontal resolution and parameterization of microphysics. *Monthly Weather Review*, *140*(1), 202–225. https://doi.org/10.1175/Mwr-D-11-00046.1

Bukovsky, M. S., & Karoly, D. J. (2010). A regional modeling study of climate change impacts on warm-season precipitation in the Central United States*. *Journal of Climate*, *24*(7), 1985–2002. https://doi.org/10.1175/2010JCLI3447.1

Carbone, R. E., Tuttle, J. D., Ahijevych, D. A., & Trier, S. B. (2002). Inferences of predictability associated with warm season precipitation episodes. *Journal of the Atmospheric Sciences*, *59*(13), 2033–2056. https://doi.org/10.1175/1520-0469(2002)059%3C2033:lopaww%3E2.0.Co;2

Chen, S. S., & Frank, W. M. (1993). A numerical study of the genesis of extratropical convective mesovortices. Part I: Evolution and dynamics. *Journal of the Atmospheric Sciences*, *50*(15), 2401–2426. https://doi.org/10.1175/1520-0469(1993)050%3C2401:ansotg%3E2.0.co;2

Cheng, C.-P., & Houze, R. A. (1979). The distribution of convective and mesoscale precipitation in GATE radar echo patterns. *Monthly Weather Review*, *107*(10), 1370–1381. https://doi.org/10.1175/1520-0493(1979)107<1370:Tdocam>2.0.Co;2

Cheruy, F., Dufresne, J. L., Hourdin, F., & Ducharne, A. (2014). Role of clouds and land-atmosphere coupling in midlatitude continental summer warm biases and climate change amplification in CMIP5 simulations. *Geophysical Research Letters*, *41*, 6493–6500. https://doi.org/10.1002/2014GL061145

Chou, M. D., and M. J. Suarez (1999). A solar radiation parameterization for atmospheric studies, 15, pp. 40, NASA Tech. Memo.
Clark, A. J., Bullock, R. G., Jensen, T. L., Xue, M., & Kong, F. Y. (2014). Application of object-based time-domain diagnostics for tracking precipitation systems in convection-allowing models. *Weather Forecasting*, *29*(3), 517–542. https://doi.org/10.1175/Waf-D-13-00098.1
Coniglio, M. C., Hwang, J. Y., & Stensrud, D. J. (2010). Environmental factors in the upscale growth and longevity of MCSs derived from rapid update cycle analyses. *Monthly Weather Review*, *138*(9), 3514–3539. https://doi.org/10.1175/2010mwr3233.1
Corfidi, S. F., Meritt, J. H., & Fritsch, J. M. (1996). Predicting the movement of mesoscale convective complexes. *Weather Forecasting*, *11*(1), 41–46. https://doi.org/10.1175/1520-0434(1996)011%3C0041:ptmomc%3E2.0.co;2
Dai, A. (2006). Precipitation characteristics in eighteen coupled climate models. *Journal of Climate*, *19*(18), 4605–4630. https://doi.org/10.1175/JCLI3884.1
Fan, J., Leung, L. R., Rosenfeld, D., Chen, Q., Li, Z., Zhang, J., & Yan, H. (2013). Microphysical effects determine macrophysical response for aerosol impacts on deep convective clouds. *Proceedings of the National Academy of Sciences of the United States of America*, *110*(48), E4581–E4590. https://doi.org/10.1073/pnas.1316830110
Fan, J. W., Han, B., Varble, A., Morrison, H., North, K., Kollias, P., et al. (2017). Cloud-resolving model intercomparison of an MC3E squall line case: Part I—Convective updrafts. *Journal of Geophysical Research: Atmospheres*, *122*, 9351–9378. https://doi.org/10.1002/2017JD026622
Feng, Z., Dong, X. Q., Xi, B. K., McFarlane, S. A., Kennedy, A., Lin, B., & Minnis, P. (2012). Life cycle of midlatitude deep convective systems in a Lagrangian framework. *Journal of Geophysical Research*, *117*, D23201. https://doi.org/10.1029/2012JD018362
Feng, Z., Dong, X. Q., Xi, B. K., Schumacher, C., Minnis, P., & Khaiyer, M. (2011). Top-of-atmosphere radiation budget of convective core/stratiform rain and anvil clouds from deep convective systems. *Journal of Geophysical Research*, *116*, D23202. https://doi.org/10.1029/2011JD016451
Feng, Z., Leung, L. R., Hagos, S., Houze, R. A., Burleyson, C. D., & Balaguru, K. (2016). More frequent intense and long-lived storms dominate the springtime trend in central US rainfall. *Nature Communications*, *7*, 13429. https://doi.org/10.1038/ncomms13429
Fritsch, J. M., Kane, R. J., & Chelius, C. R. (1986). The contribution of mesoscale convective weather systems to the warm-season precipitation in the United States. *Journal of Climate and Applied Meteorology*, *25*(10), 1333–1345. https://doi.org/10.1175/1520-0450(1986)025%3C1333:TCOMCW%3E2.0.CO;2
Fritsch, J. M., Murphy, J. D., & Kain, J. S. (1994). Warm core vortex amplification over land. *Journal of the Atmospheric Sciences*, *51*(13), 1780–1807. https://doi.org/10.1175/1520-0469(1994)051%3C1780:wcvaol%3E2.0.co;2
Gao, Y., Leung, L. R., Zhao, C., & Hagos, S. (2017). Sensitivity of U.S. summer precipitation to model resolution and convective parameterizations across gray zone resolutions. *Journal of Geophysical Research: Atmospheres*, *122*, 2714–2733. https://doi.org/10.1002/2016JD025896
Gustafson, W. I., Ma, P.-L., & Singh, B. (2014). Precipitation characteristics of CAM5 physics at mesoscale resolution during MC3E and the impact of convective timescale choice. *Journal of Advances in Modeling Earth Systems*, *6*(4), 1271–1287. https://doi.org/10.1002/2014MS000334
Hartmann, D. L., Hendon, H. H., & Houze, R. A. (1984). Some implications of the mesoscale circulations in tropical cloud clusters for large-scale dynamics and climate *Journal of Atmospheric Sciences*, *41*(1), 113–121. https://doi.org/10.1175/1520-0469(1984)041<0113:SIOTMC>2.0.CO;2
Hong, S.-Y., Noh, Y., & Dudhia, J. (2006). A new vertical diffusion package with an explicit treatment of entrainment processes. *Monthly Weather Review*, *134*(9), 2318–2341. https://doi.org/10.1175/MWR3199.1
Houze, R. A. (2004). Mesoscale convective systems. *Reviews of Geophysics*, *42*, RG4003. https://doi.org/10.1029/2004RG000150
Houze, R. A. (2014). *Cloud dynamics* (2nd ed.p. 432). Oxford: Elsevier/Academic Press.
Houze, R. A., Cheng, C.-P., Leary, C. A., & Gamache, J. F. (1980). Diagnosis of cloud mass and heat fluxes from radar and synoptic data. *Journal of the Atmospheric Sciences*, *37*(4), 754–773. https://doi.org/10.1175/1520-0469(1980)0372.0.CO;2
Houze, R. A. Jr., Rasmussen, K. L., Zuluaga, M. D., & Brodzik, S. R. (2015). The variable nature of convection in the tropics and subtropics: A legacy of 16 years of the Tropical Rainfall Measuring Mission satellite. *Reviews of Geophysics*, *53*, 994–1021. https://doi.org/10.1002/2015RG000488
Houze, R. A., Rutledge, S. A., Biggerstaff, M. I., & Smull, B. F. (1989). Interpretation of Doppler weather radar displays of midlatitude mesoscale convective systems. *Bulletin of the American Meteorological Society*, *70*(6), 608–619. https://doi.org/10.1175/1520-0477(1989)070%3C0608:Iodwrd%3E2.0.Co;2
Houze, R. A., Smull, B. F., & Dodge, P. (1990). Mesoscale organization of springtime rainstorms in Oklahoma. *Monthly Weather Review*, *118*(3), 613–654. https://doi.org/10.1175/1520-0493(1990)118%3C0613:MOOSRI%3E2.0.CO;2
Iacono, M. J., Mlawer, E. J., Clough, S. A., & Morcrette, J.-J. (2000). Impact of an improved longwave radiation model, RRTM, on the energy budget and thermodynamic properties of the NCAR community climate model, CCM3 *Journal of Geophysical Research*, *105*(D11), 14,873–14,890. https://doi.org/10.1029/2000JD900091
Janowiak, J. E., Joyce, R. J., & Yarosh, Y. (2001). A real-time global half-hourly pixel-resolution infrared dataset and its applications. *Bulletin of the American Meteorological Society*, *82*(2), 205–217. https://doi.org/10.1175/1520-0477(2001)082%3C0205:artghh%3E2.3.co;2
Kendon, E. J., Roberts, N. M., Senior, C. A., & Roberts, M. J. (2012). Realism of rainfall in a very high-resolution regional climate model. *Journal of Climate*, *25*(17), 5791–5806. https://doi.org/10.1175/JCLI-D-11-00562.1
Khain, A. P., Leung, L. R., Lynn, B., & Ghan, S. (2009). Effects of aerosols on the dynamics and microphysics of squall lines simulated by spectral bin and bulk parameterization schemes. *Journal of Geophysical Research*, *114*, D22203. https://doi.org/10.1029/2009JD011902
Klein, S. A., Jiang, X., Boyle, J., Malyshev, S., & Xie, S. (2006). Diagnosis of the summertime warm and dry bias over the U.S. Southern Great Plains in the GFDL climate model using a weather forecasting approach. *Geophysical Research Letters*, *33*, L18805. https://doi.org/10.1029/2006GL027567
Kooperman, G. J., Pritchard, M. S., & Somerville, R. C. J. (2014). The response of US summer rainfall to quadrupled CO2 climate change in conventional and superparameterized versions of the NCAR community atmosphere model. *Journal of Advances in Modeling Earth Systems*, *6*(3), 859–882. https://doi.org/10.1002/2014MS000306
Li, G., Wang, Y., Lee, K.-H., Diao, Y., & Zhang, R. (2009). Impacts of aerosols on the development and precipitation of a mesoscale squall line. *Journal of Geophysical Research*, *114*, D17205. https://doi.org/10.1029/2008JD011581
Lin, Y., Dong, W., Zhang, M., Xie, Y., Xue, W., Huang, J., & Luo, Y. (2017). Causes of model dry and warm bias over central U.S. and impact on climate projections. *Nature Communications*, *8*(1), 881. https://doi.org/10.1038/s41467-017-01040-2
Maddox, R. A. (1983). Large-scale meteorological conditions associated with midlatitude, mesoscale convective complexes. *Monthly Weather Review*, *111*(7), 1475–1493. https://doi.org/10.1175/1520-0493(1983)111%3C1475:LSMCAW%3E2.0.CO;2
Mesinger, F., Dimego, G., Kalnay, E., Mitchell, K., Shafran, P. C., Ebisuzaki, W., et al. (2006). North American regional reanalysis. *Bulletin of the American Meteorological Society*, *87*(3), 343–360. https://doi.org/10.1175/Bams-87-3-343

Morcrette, C. J., van Weverberg, K., Ma, H. Y., Ahlgrimm, M., Bazile, E., Berg, L. K., et al. (2018). Introduction to CAUSES: Description of weather and climate models and their near-surface temperature errors in 5 day hindcasts near the Southern Great Plains. *Journal of Geophysical Research: Atmospheres*, *123*, 2655–2683. https://doi.org/10.1002/2017JD027199

Morrison, H., Curry, J. A., & Khvorostyanov, V. I. (2005). A New Double-Moment Microphysics Parameterization for Application in Cloud and Climate Models. Part I: Description *Journal of Atmospheric Sciences*, *62*(6), 1665–1677. https://doi.org/10.1175/jas3446.1

Morrison, H., & Pinto, J. O. (2005). Mesoscale modeling of springtime Arctic mixed-phase stratiform clouds using a new two-moment bulk microphysics scheme. *Journal of the Atmospheric Sciences*, *62*(10), 3683–3704. https://doi.org/10.1175/Jas3564.1

Morrison, H., Thompson, G., & Tatarskii, V. (2009). Impact of cloud microphysics on the development of trailing stratiform precipitation in a simulated squall line: Comparison of one- and two-moment schemes. *Monthly Weather Review*, *137*(3), 991–1007. https://doi.org/10.1175/2008mwr2556.1

Nesbitt, S. W., Cifelli, R., & Rutledge, S. A. (2006). Storm morphology and rainfall characteristics of TRMM precipitation features. *Monthly Weather Review*, *134*(10), 2702–2721. https://doi.org/10.1175/Mwr3200.1

Powell, S. W., Houze, R. A., Kumar, A., & McFarlane, S. A. (2012). Comparison of simulated and observed continental tropical anvil clouds and their radiative heating profiles. *Journal of the Atmospheric Sciences*, *69*(9), 2662–2681. https://doi.org/10.1175/jas-d-11-0251.1

Prein, A. F., Langhans, W., Fosser, G., Ferrone, A., Ban, N., Goergen, K., et al. (2015). A review on regional convection-permitting climate modeling: Demonstrations, prospects, and challenges. *Reviews of Geophysics*, *53*, 323–361. https://doi.org/10.1002/2014RG000475

Prein, A. F., Liu, C., Ikeda, K., Bullock, R., Rasmussen, R. M., Holland, G. J., & Clark, M. (2017). Simulating North American mesoscale convective systems with a convection-permitting climate model. *Climate Dynamics*. https://doi.org/10.1007/s00382-017-3993-2

Schumacher, C., & Houze, R. A. (2003). Stratiform rain in the tropics as seen by the TRMM precipitation radar. *Journal of Climate*, *16*(11), 1739–1756. https://doi.org/10.1175/1520-0442(2003)016<1739:Sritta>2.0.Co;2

Schumacher, C., Houze, R. A., & Kraucunas, I. (2004). The tropical dynamical response to latent heating estimates derived from the TRMM precipitation radar. *Journal of the Atmospheric Sciences*, *61*(12), 1341–1358. https://doi.org/10.1175/1520-0469(2004)061%3C1341:Ttdrtl%3E2.0.Co;2

Schumacher, R. S., & Johnson, R. H. (2006). Characteristics of U.S. extreme rain events during 1999–2003. *Weather Forecasting*, *21*(1), 69–85. https://doi.org/10.1175/WAF900.1

Skamarock, W. C. (2004). Evaluating mesoscale NWP models using kinetic energy spectra. *Monthly Weather Review*, *132*(12), 3019–3032. https://doi.org/10.1175/mwr2830.1

Skamarock, W. C., J. B. Klemp, J. Dudhia, D. O. Gill, D. M. Barker, M. Duda, X.-Y. Huang, W. Wang, & J. G. Powers (2008). A description of the Advanced Research WRF version 3. NCAR Technical Note, NCAR Technical Note.

Smull, B. F., & Houze, R. A. Jr. (1987). Rear inflow in squall lines with trailing stratiform precipitation. *Monthly Weather Review*, *115*(12), 2869–2889. https://doi.org/10.1175/1520-0493(1987)115%3C2869:Riislw%3E2.0.Co;2

Stanford, M. W., Varble, A., Zipser, E., Strapp, J. W., Leroy, D., Schwarzenboeck, A., et al. (2017). A ubiquitous ice size bias in simulations of tropical deep convection. *Atmospheric Chemistry and Physics*, *17*(15), 9599–9621. https://doi.org/10.5194/acp-17-9599-2017

Steiner, M., Houze, R. A., & Yuter, S. E. (1995). Climatological characterization of three-dimensional storm structure from operational radar and rain gauge data. *Journal of Applied Meteorology*, *34*(9), 1978–2007. https://doi.org/10.1175/1520-0450(1995)034%3C1978:CCOTDS%3E2.0.CO;2

Stevenson, S. N., & Schumacher, R. S. (2014). A 10-year survey of extreme rainfall events in the central and eastern United States using gridded multisensor precipitation analyses. *Monthly Weather Review*, *142*(9), 3147–3162. https://doi.org/10.1175/MWR-D-13-00345.1

Tewari, M., Chen, F., Wang, W., Dudhia, J., LeMone, M. A., Mitchell, K., et al. (2004). Implementation and verification of the unified Noah land-surface model in the WRF model. In *20th Conference on Weather Analysis and Forecasting/16th Conference on Numerical Weather Prediction*, (pp. 11–15). Seattle, WA: American Meteorological Society.

Thompson, G., Field, P. R., Rasmussen, R. M., & Hall, W. D. (2008). Explicit forecasts of winter precipitation using an improved bulk microphysics scheme. Part II: Implementation of a new snow parameterization. *Monthly Weather Review*, *136*(12), 5095–5115. https://doi.org/10.1175/2008MWR2387.1

Thompson, G., Rasmussen, R. M., & Manning, K. (2004). Explicit forecasts of winter precipitation using an improved bulk microphysics scheme. Part I: Description and sensitivity analysis. *Monthly Weather Review*, *132*(2), 519–542. https://doi.org/10.1175/1520-0493(2004)132%3C0519:Efowpu%3E2.0.Co;2

Van Weverberg, K., Vogelmann, A. M., Lin, W., Luke, E. P., Cialella, A., Minnis, P., et al. (2013). The role of cloud microphysics parameterization in the simulation of mesoscale convective system clouds and precipitation in the tropical Western Pacific. *Journal of the Atmospheric Sciences*, *70*(4), 1104–1128. https://doi.org/10.1175/jas-d-12-0104.1

Varble, A., Zipser, E. J., Fridlind, A. M., Zhu, P., Ackerman, A. S., Chaboureau, J.-P., et al. (2014a). Evaluation of cloud-resolving and limited area model intercomparison simulations using TWP-ICE observations: 2. Precipitation microphysics. *Journal of Geophysical Research: Atmospheres*, *119*, 13,891–13,918. https://doi.org/10.1002/2013JD021372

Varble, A., Zipser, E. J., Fridlind, A. M., Zhu, P., Ackerman, A. S., Chaboureau, J.-P., et al. (2014b). Evaluation of cloud-resolving and limited area model intercomparison simulations using TWP-ICE observations: 1. Deep convective updraft properties. *Journal of Geophysical Research: Atmospheres*, *119*, 13,891–13,918. https://doi.org/10.1002/2013JD021371

Virts, K. S., & Houze, R. A. (2015). Variation of lightning and convective rain fraction in mesoscale convective systems of the MJO. *Journal of the Atmospheric Sciences*, *72*(5), 1932–1944. https://doi.org/10.1175/Jas-D-14-0201.1

Yang, Q., Houze, R. A., Leung, L. R., & Feng, Z. (2017). Environments of long-lived mesoscale convective systems over the Central United States in convection permitting climate simulations. *Journal of Geophysical Research: Atmospheres*, *122*, 13,288–13,307. https://doi.org/10.1002/2017JD027033

Yang, G. Y., & Slingo, J. (2001). The diurnal cycle in the Tropics. *Monthly Weather Review*, *129*(4), 784–801. https://doi.org/10.1175/1520-0493(2001)129%3C0784:Tdcitt%3E2.0.Co;2

Yuan, J., & Houze, R. A. (2010). Global variability of mesoscale convective system anvil structure from A-train satellite data. *Journal of Climate*, *23*(21), 5864–5888. https://doi.org/10.1175/2010JCLI3671.1

Zhang, J., Howard, K., Langston, C., Vasiloff, S., Kaney, B., Arthur, A., et al. (2011). National Mosaic and Multi-Sensor QPE (NMQ) system: Description, results, and future plans. *Bulletin of the American Meteorological Society*, *92*(10), 1321–1338. https://doi.org/10.1175/2011BAMS-D-11-00047.1

Zipser, E. J., Liu, C., Cecil, D. J., Nesbitt, S. W., & Yorty, D. P. (2006). Where are the most Intense Thunderstorms on Earth? *Bulletin of the American Meteorological Society*, *87*(8), 1057–1071. https://doi.org/10.1175/BAMS-87-8-1057